Lawrence Berkeley National Laboratory

Lawrence Berkeley National Laboratory

Title

Low Temperature Constrained Sintering of Cerium Gadolinium Oxide Films for Solid Oxide Fuel
Cell Applications

Permalink

https://escholarship.org/uc/item/4p07q00d

Author

Nicholas, Jason.D.

Publication Date

2007-06-30

Low Temperature Constrained Sintering of Cerium Gadolinium Oxide Films

for Solid Oxide Fuel Cell Applications

by

Jason Dale Nicholas

B.A. (Franklin & Marshall College) 2001

M.S. (University of Illinois at Urbana-Champaign) 2003

A dissertation submitted in partial satisfaction of the

Requirements for the degree of

Doctor of Philosophy

in

Engineering-Materials Science and Engineering

in the

Graduate Division

of the

University of California, Berkeley

Committee in charge:

Professor Lutgard C. De Jonghe, Chair

Professor Ronald Gronsky

Professor Claudia Ostertag

Spring 2007

Low Temperature Constrained Sintering

of Cerium Gadolinium Oxide Films

for Solid Oxide Fuel Cell Applications

Abstract

Low Temperature Constrained Sintering of Cerium Gadolinium Oxide Films

for Solid Oxide Fuel Cell Applications

by

Jason Dale Nicholas

Doctor of Philosophy in Engineering- Materials Science and Engineering

University of California at Berkeley

Lutgard C. De Jonghe, Chair

Cerium gadolinium oxide (CGO) has been identified as an acceptable solid oxide fuel cell (SOFC) electrolyte at temperatures (500-700°C) where cheap, rigid, stainless steel interconnect substrates can be used. Unfortunately, both the high sintering temperature of pure CGO, >1200°C, and the fact that constraint during sintering often results in cracked, low density ceramic films, have complicated development of metal supported CGO SOFCs.

The aim of this work was to find new sintering aids for $Ce_{0.9}Gd_{0.1}O_{1.95}$, and to evaluate whether they could be used to produce dense, constrained $Ce_{0.9}Gd_{0.1}O_{1.95}$ films at temperatures below 1000°C. To find the optimal sintering aid, $Ce_{0.9}Gd_{0.1}O_{1.95}$ was doped with a variety of elements, of which lithium was found to be the most effective. Dilatometric studies indicated that by doping CGO with 3mol% lithium nitrate, it was possible to sinter pellets to a relative density of 98.5% at 800°C- a full one hundred degrees below the previous low temperature sintering record for CGO. Further, it was also

found that a sintering aid's effectiveness could be explained in terms of its size, charge and high temperature mobility.

A closer examination of lithium doped $Ce_{0.9}Gd_{0.1}O_{1.95}$ indicated that lithium affects sintering by producing a Li_2O-Gd_2O_3-CeO_2 liquid at the CGO grain boundaries. Due to this liquid phase sintering, it was possible to produce dense, crack-free constrained films of CGO at the record low temperature of 950°C using cheap, colloidal spray deposition processes. This is the first time dense constrained CGO films have been produced below 1000°C and could help commercialise metal supported ceria based solid oxide fuel cells.

Table of Contents

Table Index

Figure Index

Acknowledgements

Chapter 1

Thesis Motivation, Background and Overview

1.1 Motivation

More efficient technologies are needed if the world is to meet the doubling of energy demand that is projected to occur in the next 25 years. Given the large natural reserves of hydrocarbons and the existing infrastructure, it seems likely that traditional fuels (such as gasoline and liquefied natural gas) will retain their importance, even as alternatives such as bio-fuels enter the marketplace. Thankfully, the efficiency increases possible by electrochemically reacting these fuels inside a fuel cell instead of combusting them are considerable, making it possible to lower the environmental costs associated with their continued use. For instance, solid oxide fuel cells (SOFCs) are expected to achieve first law efficiencies of 80-85% when used with cogeneration [1]; whereas, the most-efficient combustion systems used today only achieve efficiencies of 50% [2].

1.2 Fuel Cell Basics

A fuel cell utilizing an oxygen-conducting electrolyte, such as a solid oxide fuel cell, is schematically illustrated in Figure 1. Here an oxidant (usually atmospheric O_2) is added to the cathode chamber of the fuel cell where it takes on electrons and destroys oxygen ion vacancies within the electrolyte by filling them with oxygen. At the same time, fuel, such as H_2, is added to the anode chamber where it gives up two electrons forming two protons and two electrons. These protons remove oxygen from the electrolyte to make water (in the case of H_2 as a fuel) and create oxygen vacancies within the electrolyte. As

long as fuel and oxidant are provided to the fuel cell, electrons are constantly produced at the anode and constantly consumed at the cathode. This results in a voltage difference between the anode and cathode that can be used to power an electrical device. Likewise, as long as fuel and oxidant are provided to the fuel cell, oxygen ion vacancies flow through the electrolyte from the cathode to the anode. Due to the fact that oxygen diffuses through the electrolyte to the fuel compartment, oxygen-conducting electrolyte based fuel cells have the advantage of being able to oxidize a variety of gaseous fuel species (H_2, CO, CH_4). However, the large size of ionic oxygen in comparison to other ions, keeps the oxygen ion mobility low until high temperatures are reached.

Alternatively, a fuel cell can utilize a proton-conducting electrolyte, such as is the case for a phosphoric acid, solid acid, or polymer electrolyte fuel cell. These fuel cells differ from the oxygen conducting cells in that the anode to cathode electronic and ionic fluxes are inverted compared to the oxygen conductors. Further, since protons are much smaller than oxygen, the cells can be operated at lower temperature. However with this design, only pure hydrogen can be used directly as a fuel (although the hydrogen component of hydrocarbons can be used if the hydrocarbon is first broken down in a high temperature reformer).

Other fuel cell variants, such as alkaline fuel cells, which conduct OH- ions, and molten carbonate fuel cells, which conduct CO_3^{2-} ions, also exist. However, problems particular to each of these variants, such as the CO_2 poisoning of alkaline fuel cells and electrode corrosion by the molten carbonate electrolyte, has limited their appeal.

Despite the differences across the many types of fuel cells, the cell components have the same property requirements. An electrolyte must have a high ionic conductivity, a

low electronic conductivity, a low oxidant and fuel permeability, and stability in both the oxidizing and reducing environments on both sides of it. A cathode or anode must have a high ionic conductivity, a high electronic conductivity, and stability in the surrounding atmosphere. Lastly, an interconnect, which electronically links one fuel cell to another in series so that a useful voltage can be built up, must have a high electronic conductivity, a low ionic conductivity, a low oxidant and fuel permeability, and stability in both the oxidizing and reducing environments on both sides of it.

1.3 The Case for Metal Supported, Ceria Based Solid Oxide Fuel Cells

Given the unavailability of cheap, high-performance catalysts for hydrogen or hydrocarbon dissociation at temperatures below 300°C, high temperature proton and oxygen conductors seem the most likely to become mainstream devices. Of these two, solid oxide fuel cells (SOFCs) are the most studied and are the only type of fuel cell, to date, to have demonstrated stable operation up to the 70,000 hour projected stationary fuel cell operation lifetime [1].

The success of SOFCs is directly related to the high temperature functional ceramics (cathode, anode, electrolyte, and interconnect) that comprise them. These functional ceramics are ideally suited for the application for several reasons. First, the ability to tailor the ceramic electronic and ionic defect structures makes it possible to promote electrochemical reaction and transport. Second, the thermal stability of ceramics means that the breakdown of the fuel into oxidizable species (which requires elevated temperatures, if expensive catalysts are to be avoided) can occur directly inside the fuel cell, resulting in lower production costs and simpler means of operation. Lastly, the chemical stability of the ceramic material means that the corrosive impurities found in the

hydrocarbon fuel stream do not need to be eliminated, which also reduces production costs and results in simpler means of operation.

Traditionally, SOFCs have utilized a yttria stabilized zirconia (YSZ) electrolyte, a lanthanum strontium manganate (LSM) cathode, and a nickel-YSZ composite anode, as shown in Figure 1. Even though it would be beneficial to have the electrolyte as thin as possible to limit ohmic losses, the minimum thickness required to produce pin-hole free electrolytes using cheap, colloidal ceramic methods is between 5 and 15 microns. Based on these thicknesses, Steele and Heinzel [3] estimate that an electrolyte must have an ionic conductivity of at least 10^{-2} S/cm at operating temperature to be used in a real device. As shown in Figure 2, YSZ achieves this ionic conductivity near 700°C, requiring a YSZ based fuel cell to operate at or above this temperature (The oxidation reactions used in a fuel cell are generally exothermic so that once a fuel cell begins operation, maintaining a high operating temperature is not a problem.).

For many reasons it would be desirable to operate a solid oxide fuel cell at temperatures closer to 500°C. This temperature is still high enough to allow hydrocarbon oxidation without the need for precious metal catalysts, but requires less thermal insulation and allows for faster start-up times. Further, lower temperature operation also increases the voltage gained from the electrochemical reaction because:

Eqn. 1 $$\Delta G = \Delta H - T \Delta S$$

Eqn. 2 $$\Delta G = -nF \Delta E$$

where G is the Gibbs Free Energy, H is the Enthalpy, T is the Temperature in Kelvin, S is the entropy, n is the number of electrons transferred in a reaction, F is Faraday's constant and E is the voltage. Most importantly, lower temperature allows cheap stainless steel

interconnects to be introduced into the cell. Such interconnects could be load bearing members, protecting the thin ceramic anode, cathode, and electrolyte films deposited onto them from cracking. Metal incorporation into an SOFC would also permit quick and reliable joining techniques, such as welding or brazing, to be used in the production of fuel cell stacks.

Temperatures much in excess of 650°C are deleterious of metal supported SOFCs in several ways. First, at high temperatures, stainless steels suffer from excessive oxidation (especially over the 40,000 hour lifetime of the cell) that adds to the ohmic losses in the cell. Further, at high temperature chromium oxide from the steel easily vaporizes, especially if water vapor is present in the atmosphere. Chromium vaporization is problematic because the mobile chromium can chemically react with the cell components (causing a loss in fuel cell performance) or be blown out the exhaust stream (causing a potential health/environmental issue).

As shown in Figure 2, cerium gadolinium oxide (CGO) achieves the required conductivity at 500°C and could therefore be used in a metal supported fuel cell operating at this temperature.

1.4 Objectives & Experiments

Unfortunately, the development of CGO based metal supported SOFCs has been complicated by the high temperatures needed to densify CGO (>1200°C). These high temperatures promote the formation of thick, resistive iron oxide and/or chromium oxide layers that degrade the SOFC mechanically and electrically. Recent work [4] has shown that divalent dopants (Fe^{2+}, Cu^{2+}, Co^{2+}, etc.) can significantly reduce the sintering temperature of CGO. However, even today's most technologically advanced metal

supported ceria based SOFCs, which use dopants derived from the metal support to densify the CGO, are still produced at temperatures at or above 1000°C [5].[†]

Another problem complicating manufacture is that, as explained in Appendix I, porous films that are attached to a rigid substrate during densification are subjected to a tensile stress that can crack them or retard their densification.

In this work, the hypothesis that new, liquid-phase-sintering inducing sintering aids could be used to produce dense, damage-free constrained CGO films below 1000°C was evaluated. As discussed in Chapter 2, $Ce_{0.9}Gd_{0.1}O_{1.95}$ was doped with a variety of dopants, and a method for predicting a dopant's effectiveness based merely on its size, charge and high temperature mobility was developed. This analysis identified lithium as the dopant most capable of reducing the sintering temperature of $Ce_{0.9}Gd_{0.1}O_{1.95}$. Chapter 3 presents evidence that lithium lowers the sintering temperature by inducing liquid phase sintering, as hoped, and Chapter 4 details the effectiveness of this liquid in producing dense constrained CGO films. Chapter 5 summarizes all the work to date and draws some overall conclusions. Lastly, Chapter 6 discusses the obstacles remaining to the commercialization of metal supported lithium doped $Ce_{0.9}Gd_{0.1}O_{1.95}$ solid oxide fuel cells.

[†] Allowing cation migration from the steel into the electrolyte, while helpful in initially densifying the electrolyte film may be detrimental to the long-term electrical performance of the fuel cell. For instance, cation migration into the electrolyte could continue over time until a percolating, electronically-conducting network of metal atoms is established along the electrolyte grain boundaries. Therefore, it seems better to use a coating over the steel to limit the cation migration and instead introduce the dopants directly into the CGO film, as has been done in this thesis.

Chapter 2

Prediction and Evaluation of Sintering Aids for Cerium

Gadolinium Oxide

2.1 Introduction

2.1.1 SINTERING BACKGROUND

As noted earlier, of the many materials with the potential to be used as a Solid Oxide Fuel Cell (SOFC) electrolyte at intermediate temperatures of 500-700°C, Cerium Gadolinium Oxide (CGO) has one of the highest ionic conductivities [6], allowing its use in stainless steel supported fuel cells [5, 7]. However, the need to produce such cells economically at low temperature remains an issue and has prompted studies into the use of dopants and nano-sized powders to reduce the 1200°C traditionally required to densify CGO electrolytes [4, 8-23].

In addition to a very large surface area that increases the driving force for sintering, nano-powders promote low temperature sintering because, as pointed out by Herring [24], smaller particle size allows densification to occur primarily via grain-boundary diffusion instead of lattice diffusion. The flux of atoms along a grain boundary, J, may be written as:

Eqn. 3 $$J = MC\nabla\mu$$

where M is the atomic mobility along the grain boundary, C is the vacancy concentration, and $\nabla\mu$ (the gradient in the chemical potential between the particle necks and a free surface) is the driving force for sintering. Therefore, dopants that increase one or more of

these terms can, in principle, be used to lower the sintering temperature, here defined as the temperature at which a sample reaches 95% of the theoretical density under constant heating rate conditions and denoted T_{sinter}. Determining the exact manner in which a particular dopant acts can be complicated. For example, the formation of a liquid phase, which Kleinlogel and Gauckler [4] observe when CGO is doped with Co, could alter M and increase $\nabla\mu$ due to capillary effects. Dopant substitution into the near grain boundary region, which Chen and Chen [25] refer to as the undersized dopant effect and observe in Sc doped ceria, could alter M or C (especially if the atom has a charge/size discrepancy with the host ions). Lastly, dopant segregation to the grain the boundaries could alter M due to the formation of a second phase (or by scavenging SiO_2 impurities as seen by Zhang et al. [18]) or alter $\nabla\mu$ by changing the surface and interface energies.

2.1.2 DOPANT SELECTION

For an ultra-clean CGO powder such as the one used in this study, a dopant's effectiveness should simply be a matter of its ability to form a beneficial liquid phase and/or its ability to improve the CGO near grain boundary atom flux. This assumes the aforementioned dopant mechanisms are the only active ones and any secondary phase present is highly mobile at elevated temperature so that it does not become the diffusion limiting species. For a dopant to form a liquid phase, it must segregate to the grain boundaries instead of dissolving into the bulk. A dopant's solubility in the lattice is inversely proportional to the square of its "Vegard's Slope" and for CeO_2 Kim [26] showed the Vegard's Slope can be described by the equation:

Eqn. 4
$$X = (0.0220r_i + 0.00015z_i)$$

where X is the Vegard's Slope, r_i is the difference in ionic radii between the dopant and Ce^{4+} in 8-fold coordination, and z_i is the difference in charge between the dopant and Ce^{4+}. A plot showing the good fit of this equation to soluble CGO dopants is shown in Figure 3. Hong and Virkar [27] have developed a similar expression for the Vegard's Slope, and Ranlov et al. [28] have shown the relationship between the Vegard's Slope and the solubility even holds for nearly insoluble CGO dopants, as shown in Figure 4. Because of the requirement that a liquid-forming dopant possess a low solubility in the bulk, the dopants most likely to induce liquid phase sintering in CGO should be those with an absolute value of the Vegard's Slope >> 0. That said, as may be the case for Si [29] and Al [8] as shown in Table 1, if the |Vegard's Slope| is too large, a second phase in which CGO is insoluble can form preventing liquid phase sintering and forcing the system to sinter via the solid-state sintering mechanism observed for the pure material (As noted by Kingery [30], one of the requirements for liquid phase sintering is that the solid phase be soluble in the liquid so that atom transport can occur). Therefore, dopants with moderate absolute values of the Vegard's Slope should be the most likely to induce liquid phase sintering in CGO, such as the known cases of Bi^{3+} [9] and Co^{2+} [10].

Furthermore, the idea of using the Vegard's Slope as a sintering aid quality factor extends beyond liquid phase sintering. Ideally, a sintering aid would both form a beneficial liquid phase and favorably alter the near grain boundary, solid-state atom flux as well. Chen and Chen [31] showed that in CeO_2, cations are the limiting diffusing species, which is understandable given the material's high oxygen mobility. As illustrated in Figure 5, they also showed that undersized acceptor dopants substantially increase the near grain boundary cation mobility by increasing the near grain boundary vacancy concentration

(due to charge compensation and the preference of an undersized dopant to coordinate with fewer than eight oxygen atoms) while expanding the oxygen coordination shells around the host cations. Unfortunately, the relative importance of dopant size versus dopant charge on the near grain boundary cation mobility has never been explicitly stated, making it difficult to identify those dopants that increase the near grain boundary atom flux. However, the Vegard's Slope quality factor provides exactly that. Since oxygen vacancies and oxygen sub-lattice relaxation relieve strain within the lattice, their concentration in the near-grain boundary region should be proportional to the increase in strain energy caused by both a dopant's charge and size, which is described by the Vegard's Slope via the relations,

Eqn. 5 $$W = 6Ga_o(\Delta a)^2$$

Eqn. 6 $$\Delta a = Xm_i$$

where W is the strain energy, G is the shear modulus, a_o is the initial lattice parameter, Δa is the change in lattice parameter caused by dopant substitution, X is the Vegard's Slope calculated from Eqn. 4, and m_i is the concentration of soluble dopant [26]. Thus, dopants with a positive Vegard's Slope (atoms which are oversized, electron donating, or both) should decrease the near-grain boundary oxygen-ion vacancy concentration and therefore increase the solid-state sintering temperature, while dopants with a negative Vegard's Slope (atoms which are undersized, electron accepting, or both) will have the opposite effect.

In summary, using the Vegard's Slope equation (Eqn. 4) and a knowledge of a dopants size and charge, it should be possible to identify the moderately undersized acceptor dopants most likely to induce low temperature sintering in CGO through either liquid phase sintering or a modification of the near grain boundary atom flux. In this study,

the densification behavior of $Ce_{0.9}Gd_{0.1}O_{1.95}$ doped at the 1, 3 and 5mol% level with 11 different cations (see highlighted entries in Table 1) was examined to test this hypothesis. The oxygen ion conductivity and the final grain size were also determined for samples doped at the 3mol% level. This is the first time a single batch of powder has been used to study such a wide range of CGO dopants, allowing a direct comparison of dopant effectiveness.

2.2 Experimental

Dopant amounts were calculated assuming equal substitution for Ce and Gd, no Ce reduction to the 3^+ oxidation state, and charge compensation by oxygen. For example, the composition assumed for 3mol% Li was $Li_{0.03}Ce_{0.873}Gd_{0.097}O_{1.9065}$ and the composition assumed for 1mol%Al was $Al_{0.01}Ce_{0.891}Gd_{0.099}O_{1.9455}$. Appropriate amounts of 99.999% pure nitrates (Alfa Aesar) were weighed, after accounting for the water of hydration as determined by ICPMS, and dissolved in ~200mL of solvent (either water or ethanol) using a magnetic stirbar. Appropriate amounts of nano-sized ultra high surface area ($7\text{-}10m^2$/g) $Ce_{0.9}Gd_{0.1}O_{1.95}$ powder (Rhodia) were then added to the nitrate solutions and the solvent was removed over the course of several hours of stirring. TEM analysis of the as-received CGO powder, shown in Figure 6, showed it to be made of equiaxed ~40nm grains agglomerated into lenticular masses 75nm wide and 600nm long. After solvent removal, the powders were dried at 130°C for a minimum of four hours to drive off any surface water. The mixture was then ground in an alumina mortar and pestle, sieving through a 150 micron stainless steel mesh, and 1.242 (±0.003)g of each mixture was uxiaxially pressed to 4.5 (±0.1) kpsi inside a ½ inch steel die.

Uniaxial pushrod dilatometry at 4°C/min in air was conducted using a Model 1600 Orton Dilatometer. The near constant height of the sample pellets, 0.116-0.126 inches, ensured that the dilatometer spring force was constant for all samples. The thermal-expansion-corrected relative density was calculated from the percent linear shrinkage (PLC), $(l-l_0)/l_o$ x 100 in the measurement direction, assuming uniform densification, no mass loss, and zero creep according to the equation:

Eqn. 7
$$\% \, Relative \, Density = \frac{\rho_{initial} * 100}{\rho_{theoretical}(temp)*\left(1+\frac{PLC(temp)}{100}\right)^3}$$

where ρ represents the density, as derived in Appendix II. The theoretical density of the doped CGO was assumed to be sufficiently close to that of pure CGO so that $\rho_{theoretical}(temp)$ for the doped material could be approximated by that of the pure material. Even though there have been literature reports of dopants affecting the thermal expansion of $Ce_{0.9}G_{0.1}O_{1.95}$ [32], the effect is so small that it is insignificant on a plot dominated by sintering induced relative density changes. The $\rho_{theoretical}(temp)$ of the pure material was found through a dilatometric measurement of the thermal expansion of a dense, pure CGO pellet using the equation:

Eqn. 8
$$\rho_{\text{theoretical of CGO}}(temp) = \frac{\rho_{\text{theoretical of CGO at 25C}}}{\left(1+\frac{PLC_{\text{of Pure Dense CGO as a function of temp}}}{100}\right)^3}$$

The theoretical room temperature density for pure $Ce_{0.9}G_{0.1}O_{1.95}$ was calculated from literature reports of the room temperature lattice parameter [32] and the atomic weights of Ce, Gd, and O to be $7.23 g/cm^3$.

To prevent contamination, each dopant nitrate had a dedicated stirbar and beaker, new alumina spacers were used for each dilatometer run, and the dilatometer was cleaned by firing high surface area alumina for more than 12 hours at 1500°C after runs containing high vapor pressure dopants such as Li and K. Further, throughout the course of the experiments, dilatometer performance was evaluated by measuring a pure CGO sample. Some dilatometry runs were also conducted more than once to ensure consistency.

To determine the grain size, the sintered pellets were polished down to 0.25 microns using SiC sandpaper and diamond lapping films. The samples were then thermally etched by heating to 1300°C at 10°C/min, holding for 20 minutes, and cooling at 10°C/min. This thermal etch was one hundred degrees below the initial sintering temperature and therefore should not have significantly altered the microstructure. After being gold coated, the samples were analyzed in a scanning electron microscope. The resulting images were thresholded, and the grain size was analyzed using Adobe Photoshop and the Image Processing Toolkit 5.0 plug-ins.

To determine the oxygen ion conductivity, samples were sanded and gold electrodes were deposited by sputtering. The samples were then placed in a spring-loaded push-contact furnace apparatus, and preheated to 200°C. After equilibrating at 200°C for at least 30 minutes, a two-point conductivity test was conducted by measuring samples' impedance vs. frequency behavior from 1×10^{6} to 1Hz using a Solartron 1260 Impedance/Gain Phase Analyzer. A detailed explanation of how the ionic conductivity was determined from the AC Impedance spectra can be found in Appendix III.

2.3 Results

Results from the dilatometry experiments are shown from Figure 7-Figure 20. The ionic conductivity and average grain sizes from samples doped at the 3mol% level are shown in Table 3 and Figure 8, respectively. Even though some creep is present during dilatometry (hence the apparent densities >100%), as shown in Table 4 the dilatometry curves represent mainly densification as determined by comparing the total post-experiment dilatometric strain (which is assumed to represent the linear combination of densification strain and the creep strain) to the actual post-experiment densification strain (determined by measuring the sintered pellet dimensions and use of the equation:

Eqn. 9
$$\varepsilon_{Densification} = \frac{1}{3}\left(\varepsilon_{axialdirection} + 2\varepsilon_{radialdirection}\right).$$

The only other non-densification related changes shown in the dilatometer curves are the apparent reduction in density for copper doped CGO above 1000°C, and iron and manganese doped CGO above 1300°C. This behavior for copper doping was also seen by Kleinlogel and Gauckler [33] who propose it is the result of the reactions:

Eqn. 10
$$4CuO \xrightarrow{1027°C} 2Cu_2O + O_2 \xrightarrow{1124°C} liquid$$
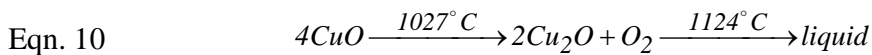
Based on thermodynamic transition temperatures [34], the fact that iron and manganese nitrate decompose into Fe_2O_3 [35] and Mn_2O_3 [36], and the oxide densities shown in Table 2, it seems likely the high temperature drops in apparent density seen in the iron and manganese curves are not actual drops in CGO density but the result of a lower density dopant oxide phase forming via the reactions:

Eqn. 11
$$6Fe_2O_3 \longrightarrow 4Fe_3O_4 + O_2$$

Eqn. 12 $$6Mn_2O_3 \longrightarrow 4Mn_3O_4 + O_2$$
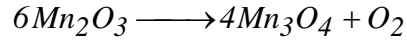
2.4 Discussion

As shown in Figure 8, and confirmed by subsequent firings, by doping $Ce_{0.9}Gd_{0.1}O_{1.95}$ with 3mol% Li it is possible to sinter $Ce_{0.9}Gd_{0.1}O_{1.95}$ at 800°C for 1 hour to a density of 98.5%. This is the lowest sintering temperature ever recorded for CGO and it suggests it may be possible to produce a metal supported SOFC at temperatures below the 1000°C currently used [5] by doping CGO with Fe (which migrates from the steel support). Figure 7, Figure 8, and Figure 9 show that Co, Cu, Fe, Mn and Zn were also able to reduce the sintering temperature of $Ce_{0.9}Gd_{0.1}O_{1.95}$ at the 1, 3 and 5mol% dopant levels. Interestingly, all of these beneficial dopants (Co, Cu, Fe, Mn, Zn, and Li) have a Vegard's Slope between –45 and –58, confirming that slightly soluble, moderately undersized acceptors make the best CGO dopants, as expected. Al with a Vegard's Slope of –77 inhibited sintering, presumably through the formation of a low mobility secondary oxide at the grain boundaries as has been seen elsewhere [8]. Being right on the poor-solvent, second phase borderline with a Vegard's Slope of –61, but with a high mobility of that second phase as shown in Figure 21, Ni failed to influence sintering in either direction. As expected, Ca, with a Vegard's Slope of 3, did not differ significantly from the pure CGO curve, and K, with a Vegard's Slope of 74, inhibited sintering.

The only dopant to disobey its Vegard's Slope prediction was Mg. With a Vegard's Slope of –48, Mg should have reduced the sintering temperature instead of inhibiting it slightly. However, in light of Figure 21, it seems likely the poor sintering resulted from Mg replacing the host cations (Ce and/or Gd) as the diffusion limiting species. This

hypothesis is supported by the study of Chen and Chen [25] who found that at low dopant levels Mg promoted grain growth in pure ceria through an undersized dopant effect, but at dopant levels of 1mol% and greater Mg inhibited grain growth through a solute drag effect. Figure 21 also helps explain the superior performance of lithium which posses both a high vapor pressure and a low Vegard's Slope. Thus, it seems that in addition to being a moderately undersized acceptor dopant, a good sintering aid also has a high vapor pressure (or a high mobility for some other reason).

The influence of a particular dopant on the oxygen ion conductivity and the average grain size can be seen in Table 3 and Figure 22, respectively. Table 3 shows that as expected, dopants with a |Vegard's Slope| >> 0 did not enter the crystal structure and affect the lattice oxygen ion conductivity. Table 3 also suggests that for some samples doped at the 3mol% level, active steps should be taken to remove the dopants after sintering so that the grain boundary oxygen ion conductivity is not reduced below usable levels. That said, Avila-Paredes and Kim [37] reported that Cu, Mn, Fe and Co at the 1mol% level actually reduced the grain boundary resistance, suggesting complete dopant removal may not be necessary. The very large grain sizes of the 3mol% Cu and Li doped samples seen in Figure 22 suggest that a liquid is present in these systems during sintering. Although these grain sizes are quite large, it is expected that sintering at the reduced temperatures allowed by these dopants will result in much lower grain size.

Table 5 shows that the dilatometry results agree well with literature reports. For those cases were it does not, the results can be explained by the difference in CGO Gd content. Co-doping with Gd should increase sintering aid solubility, and therefore lower the sintering temperature, since the increase in oxygen vacancy concentration caused by

the additional Gd should relieve more of the lattice strain caused by the sintering aid entering the crystal structure. As expected, in those cases where the Gd doping level is higher than this study, ref. [8] in the case of Al and ref. [4] in the case of Ni, the sintering aid is reported to be more beneficial than in this study. Further, in those cases where the Gd doping level is less than this study [38], i.e. for Mg and Ca, the sintering aid is reported to be less beneficial than in this study.

Lastly, all the beneficial dopants in this study had Vegard's Slopes between –45 and –58 suggesting it might be possible to identify new beneficial dopants other than those available commercially as nitrates as listed in Table 1. Such dopants could be introduced via the glycine-nitrate combustion [39] or some other technique. The lower limit of this Vegard's Slope criteria, -58, is well defined given the propensity of dopants with a Vegard's Slope less than this to form liquids in which $Ce_{0.9}Gd_{0.1}O_{1.95}$ is insoluble, as evidenced by the behavior of Ni. However, the upper limit of –45 simply resulted from the choice of dopants evaluated in this study. Thus, consideration of all high vapor pressure dopants with a Vegard's Slope of, say, -30 to -58, regardless of whether they have a commercially available nitrate or not, may identify new dopants capable of inducing low temperature sintering in ceria. However, given its high vapor pressure and very negative Vegard's Slope it seems likely lithium will remain the most effective dopant for inducing low temperature sintering in ceria.

2.5 Conclusions

In conclusion, with only knowledge of the Vegard's Slope equation for the host material, the high temperature vapor pressure of the dopant oxide, and the Shannon ionic radii tables [40], it is possible to identify the dopants most likely to induce the low

temperature sintering of $Ce_{0.9}Gd_{0.1}O_{1.95}$. This is the first time the Vegard's Slope has been used in this way. Using a single batch of powder, a direct evaluation of dopant effectiveness was conducted and the beneficial sintering aids had a high vapor pressure at elevated temperature and a Vegard's Slope between –45 and –58. In particular, Li doped CGO sintered to near full density at a remarkably low 800°C. This record-low sintering temperature may allow for the production of metal supported ceria SOFCs at temperatures below the 1000°C commonly used today, and this Vegard's Slope quality factor analysis may prove useful for identifying beneficial sintering aids in other systems.

Chapter 3

Liquid Phase Sintering of Lithium Doped $Ce_{0.9}Gd_{0.1}O_{1.95}$

3.1 Introduction

Due to it's high oxygen ion conductivity at intermediate (500-700°C) temperature and potential use as a commercial solid oxide fuel cell (SOFC) electrolyte, many investigators[4, 8-23] have sought to densify $Ce_{0.9}Gd_{0.1}O_{1.95}$ (CGO) at low temperature using sintering aids. In Chapter 2, it was argued that a sintering aid's ability to promote densification by 1) increasing the grain boundary oxygen vacancy concentration (an effect commonly known as the undersized dopant effect) and/or 2) forming a liquid or intergranular phase was fundamentally a matter of a dopant's size and charge and could be summarized in terms of a Vegard's Slope quality factor. Using this Vegard's Slope analysis, lithium was predicted to be a good CGO sintering aid and experiments revealed that despite the fact that pure nano-sized CGO requires 1200°C to reach full density, nano-sized CGO doped with as little as 3mol% lithium nitrate could be sintered to 98.5% density at the record low temperature of 800°C. In the literature there is currently a debate over whether CGO sintering aids act by increasing mass transport in the grain boundary cores through the formation of liquids/sub-eutectic intergranular films [4, 41], or whether they act in the space charge layers within the grains through an alteration of the grain boundary oxygen vacancy concentration [16, 20]. This chapter presents data indicating that a liquid phase sintering mechanism is active in lithium nitrate doped CGO.

3.2 Experimental

3.2.1 SAMPLE PREPARATION

Samples were prepared by mixing appropriate amounts of 99.999% pure soluble dopants salts (Alfa Aesar) with a single batch of commercially available, nano-sized, ultra high surface area (7-10m^2/g) $Ce_{0.9}Gd_{0.1}O_{1.95}$ powder (Rhodia) in either water or ethanol. After removing the solvent by stirring for several hours with a magnetic stirbar, the powders were heated to ~130°C for a minimum of 4 hours using either with a heatlamp or a muffle furnace to drive off any residual water. Dopant amounts were calculated assuming Ce remained in the 4^+ oxidation state, equal dopant substitution for Ce and Gd, and charge compensation by oxygen. For example, the assumed composition for 3mol% Li-CGO was $Li_{0.03}Ce_{0.873}Gd_{0.097}O_{1.9065}$. Transmission Electron Mircroscopy (TEM), X-ray Diffraction (XRD), and light scattering based Particle Size Analysis (PSA) showed the as-received powders to be made of equiaxed ~40nm grains agglomerated into lenticular masses 75nm wide and 600nm long, as shown in Figure 6.

3.2.2 DILATOMETRY

In preparation for dilatometry, the powders where ground in an alumina mortar and pestle, sieved through a 150 micron stainless steel mesh, and 1.250 (+/- 0.005)g of powder was pressed to 4.5 (±0.1) kpsi using a ½ inch steel die. Uniaxial pushrod dilatometry was conducted using an Orton 1600 dilatometer and a heating rate of 4°C/min from room temperature to 1400°C in air. To prevent contamination, new alumina dilatometer spacers were used for each experiment. To gain a sense of how much of a dilatometry curve represented densification versus creep, the total amount of creep for each sample was

determined using the procedure described in Chapter 2. After sintering, a variety of characterization methods, discussed below, were employed.

3.2.3 ELECTRICAL CHARACTERIZATION

For conductivity measurements, samples were ground flat and parallel, sputtered with ~50nm of Au or Pt, and placed into a spring-loaded push-contact furnace apparatus. The oxygen ion conductivity as a function of temperature was then determined based on the sample dimensions and the AC Impedance versus frequency curves, as discussed in Appendix II. The Impedance spectra were collected from 5×10^6 Hz to 0.1Hz using a Solartron 1260 Impedance/Gain Phase Analyzer after at least 30 minutes of thermal equilibration.

3.2.4 COMPOSITIONAL AND MICROSTRUCTURAL ANALYSES

To analyze the grain size, Scanning Electron Microscopy (SEM) was conducted inside a FEI Strata 235 dual beam focused ion beam operating at 30kV on samples sputtered with ~20nm of Au and held in an aluminum holder.

Powder XRD scans were collected using a Siemens D-500 diffractometer on mixtures produced by grinding samples and a titanium reference powder in an alumina mortar and pestle. Following collection, the XRD spectra were run through a noise reduction filter and the position of the entire spectra were adjusted by at most 0.1° to align the Ti peaks.

TEM samples were prepared by polishing, dimpling, and cryogenic ion milling. To eliminate charging in the electron microscope, a 20nm thick layer of graphite was evaporated onto the sample surface. Transmission electron microscopy was conducted

using a Phillips CM200/FEG microscope, operating at 200kV. The point resolution of this microscope was 0.23nm and the information limit was 0.16 nm. Chemical composition analysis was conducting using Energy Dispersive X-ray Spectrocopy (EDS).

Lastly, X-ray Photoelectron Spectroscopy (XPS) was conducted using custom built system located in the Lawrence Berkeley National Laboratory Molecular Foundry.

3.3 Results

Dilatometry results for $Ce_{0.9}Gd_{0.1}O_{1.95}$ doped at the 1, 2, 3, 4, 5 and 15mol% lithium nitrate levels are shown in Figure 23. As presented in Chapter 2, this plot shows that with as little as 3mol% lithium nitrate, dense CGO pellets can be produced at 800°C. As shown in Table 6, the dilatometric strains for the 1-5mol% lithium nitrate doped samples are mainly due to densification processes, while the 15mol% $LiNO_3$ doped CGO sample shows a significant amount of both creep and densification. During dilatometry, the 15mol% $LiNO_3$ doped CGO sample bonded tightly to the alumina spacers. Dilatometry plots for CGO samples doped with various lithium salts at the 3mol% level, and the accompanying strain information, are shown in Figure 24 and Table 7, respectively, indicating that lithium nitrate is the optimal lithium dopant.

As shown in Figure 25, the initial total oxygen ion conductivity of a 3mol% $LiNO_3$ doped CGO sample fired at 800°C for 1 hour was 1.5 orders of magnitude lower than undoped CGO. This was due to a grain boundary effect as the lattice conductivity, observed at 200 and 300°C but not shown in Figure 25, was equal to that of the pure material. Heating past 400°C caused an order of magnitude reduction in the oxygen ion conductivity. This reduction in magnitude took approximately 60 minutes to reach a steady

state value. Upon continued heating to 700°C and subsequent cooling to room temperature the conductivity followed a different path than during heating, although the activation energies for the initial and reduced conductivities were roughly similar. Subsequent reheating of the sample from room temperature to 300°C (data not shown in Figure 25) resulted in a conductivity identical to the one seen at 300°C during cooling. However, after the sample's original electrodes were removed and new ones applied, the conductivity returned to that seen initially during heating. This suggests the formation of an insulating second phase at the sample-electrode interface. As before, heating above 400°C resulted in a conductivity discontinuity and the sample followed a different path upon cooling.

The microstructures of a pure and 3mol% $LiNO_3$ doped CGO sample fired to 1400°C, polished down to a 1micron grit size using diamond lapping film, and thermally etched for 20 minutes at 1300°C are shown in Figure 26 and Figure 27 respectively. Also, a 3mol% $LiNO_3$ doped CGO sample was fired to 800°C, polished down to a 1micron grit size using diamond lapping film, and thermally etched for 20 minutes at 750°C. During polishing of this sample some regions polished nicely while others had a significant amount of pluck-outs suggesting the presence of a mechanically weak intergranular film. Further, thermal etching at 750°C caused a liquid film shown in Figure 28 to extrude from the surface and obstruct the grains beneath.

XRD Spectra for as-received un-fired CGO, and 15mol% lithium nitrate doped CGO fired for 1 hour at 800°C are shown in Figure 29. As shown in the close-ups, the addition of lithium had no effect on the CGO lattice parameter.

Figure 30 shows some transmission electron micrographs for a pure, pre-densified (98% dense) CGO pellet fired for 1 hour at 800°C in a lithium-saturated atmosphere. The

atmosphere was lithium saturated by surrounding the sample with an equal volume of unfired 15mol% $LiNO_3$ doped CGO powder, and placing an alumina lid over the powder and sample during sintering. Approximately 2/3 of the grain boundaries, as shown in Figure 30.a, were identical to those seen in a normal pure CGO sample. However, approximately 1/3 of the boundaries contained an amorphous intergranular film, as shown in Figure 30.b and Figure 30.c. Over and under focusing of the microscope ensured that these were intergranular films, and not simply edge effects. EDS scans of the grain and the (grain + grain-boundary) regions detected only Ce, Gd, and O peaks, but indicated the grain boundary was slightly Gd enriched. It was not possible to detect lithium in the sample using either EDS or EELS.

15mol% $LiNO_3$ doped CGO bulk samples were also sintered in a muffle furnace at 800°C for 1 hour (as opposed to the dilatometer). During firing a colorless, transparent phase ~0.7mm in thickness was extruded from the sample. EDS analysis on a piece of this phase plucked from the surface detected only oxygen, while XPS analysis, shown in Figure 31, revealed the phase to be comprised most of lithium and oxygen with a minor amount of Ce and Gd.

3.4 Discussion

3.4.1 EVIDENCE FOR THE PRESENCE OF A HIGH TEMPERATURE LIQUID PHASE IN LITHIUM NITRATE DOPED CGO

Several pieces of evidence suggest an intergranular liquid phase is present at high temperature in $LiNO_3$ doped CGO. First, lithium remains at the grain boundaries instead of dissolving in the bulk, and is therefore available to form an intergranular liquid when

heated. The decrease in the oxygen-ion grain boundary conductivity and constancy of the lattice grain boundary oxygen ion conductivity with doping, shown in Table 3, suggests that lithium remains at the grain boundaries, as does the Vegard's Slope analysis, and the identical lattice parameters for the pure and lithium doped samples shown in Figure 29. Second, an amorphous intergranular film, which could very likely have been a liquid at high temperature, is present in sintered samples, as shown in the TEM images of Figure 30. Third, the conductivity discontinuity seen above 400°C is also consistent with a liquid collecting at the electrode-electrolyte interface. Lastly, the lithium rich second phase found atop the 15mol% $LiNO_3$ doped CGO sample, described in Figure 28 and Figure 31, is reminiscent of the liquid extrusion during sintering seen in other systems such Mg doped zirconia [42]. Unfortunately, the nature of the Li_2O-CeO_2-Gd_2O_3 phase relations at high temperature are unknown at this time, but the collection of such a large quantity of material on the sample surface suggests the presence of a true liquid phase, and not simply a sub-eutectic intergranular film.

3.4.2 EVIDENCE FOR LIQUID PHASE SINTERING

The effectiveness of this lithium-rich high temperature liquid in promoting sintering is illustrated most clearly in the dilatometry curves of Figure 23. The incredibly large amount of densification over just the course of a few minutes, seen near 950°C for the 1-2mol% Li-CGO and near 800°C for higher lithium doping levels, is indicative of the fast transport pathways provided by a liquid phase, as is the large grain sizes for $LiNO_3$ doped CGO shown in Figure 26. Further, the observation that the 15mol% Li-CGO sample begins to strain at a much lower temperature than the other dopant levels suggests liquid phase sintering. For if Li-CGO was straining solely via an undersized dopant mechanism,

once the space charge region was saturated with dopant, further additions of dopant should either retard sintering, in the event the non-soluble dopant had a low mobility, or have little effect on sintering, in the event the non-soluble dopant had a high mobility. However, lithium, which has almost no solubility in CGO, shows a continual decrease in the sintering initiation temperature as the dopant level is increased to 15mol%, presumably due to increased quantities of liquid aiding in the initial particle rearrangement.

3.4.3 IDENTITY OF THE LIQUID RESPONSIBLE FOR LOW TEMPERATURE SINTERING IN LITHIUM NITRATE DOPED CGO

Given the XPS analyses shown in Figure 31, it seems likely that the liquid/intergranular film responsible for the low temperature sintering of CGO is Li_2O in which small amounts of cerium and gadolinium are soluble.

3.5 Conclusions

From a practical standpoint, this work shows that 3mol% lithium nitrate is the optimum lithium dopant quantity and form, capable of producing dense CGO pellets at the record low temperature of 800°C. It shows that across all dopant levels, lithium remains at the grain boundaries instead of dissolving into the CGO and this, coupled with the fact that at elevated temperature this grain boundary film lowers the oxygen ion conductivity, indicates that steps must be taken to remove the lithium after sintering to ensure hassle-free SOFC device operation.

From a mechanistic standpoint, the presented evidence shows that a liquid is present at temperatures greater than 400°C in lithium nitrate doped CGO, that this liquid aids in the low temperature sintering of lithium nitrate doped CGO, and that this liquid is

most likely a eutectic liquid formed close to the Li_2O end member in the Li_2O-CeO_2-Gd_2O_3 system. Further, an increase in the near-grain boundary lattice flux that would occur as a result of undersized dopants creating more oxygen vacancies is not needed to explain the observed phenomenon. However, this sintering mechanism could be operating in parallel with the observed liquid phase sintering mechanism.

Chapter 4

Constrained $Li_{0.03}Ce_{0.873}Gd_{0.097}O_{1.9065}$ Electrolyte Film Densification at Low Temperature

4.1 Introduction

In an effort to commercialize solid oxide fuel cells (SOFCs), many groups are pursuing the development of stainless steel supported SOFCs capable of operating at temperatures as low as 500C. Presently, these SOFCs employ a dense $Ce_{0.9}Gd_{0.1}O_{1.95}$ electrolyte to conduct oxygen ions and impede the flow of electrons and gases. Due to the low cost of using colloidal methods to deposit porous films and the desire for near net shape manufacturing, the ability to produce a dense constrained CGO film atop an invariant substrate by first colloidally depositing the film and then using a heat treatment to densify it would be very advantageous. Unfortunately, as shown by Scherer and Garino [43] constraint by a rigid substrate produces a tensile stress, which opposes sintering and often results in a cracked and/or low density film. Another difficulty in producing dense CGO films on metal supports is the fact that even nano-sized, unconstrained $Ce_{0.9}Gd_{0.1}O_{1.95}$ doesn't sinter to full density until 1200°C, as shown in Figure 8. This can be problematic for sintering CGO on a stainless steel support because at temperatures greater than 1000°C excessive oxidation and extreme chromium diffusion can occur.

One option, which is employed in the manufacture of metal supported yttria stabilized zirconia solid oxide fuel cells, is to allow the porous metal support to shrink with the densifying ceramic, at the expense of not being able to produce a near net shape

component [44]. Another option is to use arc plasma spraying to deposit the electrolyte layer onto a rigid substrate [45]. However, the difficulty in producing a completely gas tight electrolyte layer and the expense are disadvantages of this technique. A third option, and the one currently used by Ceres Power, Ltd, is to colloidally deposit CGO onto an rigid metal support and allow iron and manganese migration from the substrate to aid in densification of the CGO electrolyte [5, 46].

The reason this third option works is because, as originally shown by Kleinlogel and Gauckler, the addition of small amounts of transition metals such as Fe and Mn reduce the sintering temperature of unconstrained CGO to as low as 900°C [4]. TEM and/or dilatometry results on Fe [47], Mn [16], and Co doped CGO [4, 41] suggest that, at least during the initial stages of sintering, a liquid-like intergranular film forms which helps densify the ceramic. For Fe doped CGO, the liquid-like intergranular film allows the constrained film to sinter at temperatures as low as 1000°C [5]. As described by Scherer and Garino[43] and derived in Appendix I, the normalized densification rate for such a film is given as:

Eqn. 13

$$\left(\frac{\dot{\rho}}{\rho}\right) = \dot{\varepsilon}_{Free}(\rho)\left(\frac{1+\nu(\rho)}{1-\nu(\rho)}\right)$$

where σ is the stress, E is the viscosity, $\dot{\varepsilon}$ is the strain rate of the unconstrained ceramic, ρ is the density, and ν is the viscous poisson ratio. At high temperature, liquids aid in the densification of constrained films by lowering the film viscosity, increasing the film's viscous poisson ratio, producing a compressive capillary stress, and lubricating the particles during initial particle rearrangement.

Through the studies presented in Chapter 2 and Chapter 3, unconstrained $Ce_{09}Gd_{0.1}O_{1.95}$ was sintered to full density at 800°C using lithium as a dopant instead of the 1100°C required with the use of iron or manganese. This suggested it might be possible to constrain sinter CGO at temperature below 1000°C using Li as a dopant since lithium doped CGO undergoes liquid phase sintering. In this chapter, this possibility was investigated.

4.2 Experimental

The composition $Li_{0.03}Ce_{0.873}Gd_{0.097}O_{1.9065}$ was chosen for this study because, as shown in Figure 23, it is the minimum amount of dopant required to ensure densification at 800°C for unconstrained samples. The doped powder was prepared by dissolving the appropriate amount of 99.995% pure lithium nitrate (Alpha Aesar), taking into account the waters of hydration, in ~200mL of distilled water, and then adding the appropriate amount of ultra high surface area (7-10m^2/g) $Ce_{0.9}Gd_{0.1}O_{1.95}$ (Rhodia) under constant stirring. The water was removed by stirring the solution for several hours under a fan and heatlamp. The resulting powder was calcined at 500°C for 1 hour. Ball milling charges were prepared by first dissolving 0.2g of dibutyl phthalate, which served as a dispersant, in ~15mL of 2-propanol. This solution, 5.0g of calcined Li-CGO powder, and ~35g of 3mm yttria stabilized zirconia balls were added to a 40mL polyehtelene bottle, the bottle was sealed and rotated at 55rpm for 24 hrs. After pouring the milling charge through a sieve to collect the YSZ milling balls, the suspension was reduced to a 1 wt% solids loading through the addition of 2-propanol, and the suspension was sonicated for 5 minutes in an ice water bath. The Li-CGO suspension was then airbrushed onto a series of 98% dense

$Ce_{0.9}Gd_{0.1}O_{1.95}$ preheated to ~300°C over the course of an hour to produce a porous film 30-50 microns thick. A tape-casting mylar sheet containing an anti-stick coating was then placed over each film and the samples were cold-isostatically pressed at 2kpsi to densify the film. Lastly, the samples were placed on an alumina plate and surrounded by ~2g of unfired 15mol% Li-CGO powder and fired. An alumina cover that extended over both the sample and the 15mol% Li-CGO powder limited gas exchange during firing and ensured the sample atmosphere remained lithium saturated. The heating rate for all samples was 4°C/min and the nominal cooling rate was 10°C/min, although the actual cooling rate at low temperature was known to be longer due to the thermal inertia of the oven.

After firing the samples were sectioned, polished down to a 1-micron grit size using SiC sandpaper and diamond lapping film, and the microstructure was analyzed in a JEOL JSM6340F scanning electron microscope (SEM) operating at 20kV or a FEI Strata 235 dual beam scanning electron microscope/focused ion beam (SEM/FIB) operating at 30kV. In some cases, the samples were crossed section using the focused ion-beam to determine the grain size and/or porosity. Grain size analysis was determined using Adobe Photoshop and the Image Processing Toolkit.

4.3 Results & Discussion

Figure 32 shows that pure, pressed CGO films constrained by a rigid substrate cannot be densified even by firing at 1400°C for 4 hours. Un-pressed Li-CGO films fired at 1400°C for four hours in a lithium saturated atmosphere, and pressed Li-CGO films fired at 1400°C for four hours in an atmosphere that was not lithium-saturated were all porous. This indicates that reducing the strain to full density by pressing, and preventing

lithium loss during firing are critical sintering parameters. By firing pressed lithium doped films in a lithium saturated atmosphere, as shown in Figure 33 and Figure 34, it is possible to constrain sinter CGO to full density on an inert (meaning that the substrate does not provide dopant elements to the film) substrate at the record low temperature of 950°C. Li-CGO films fired at this record low 950°C for four hours had an average grain size of 1.78μm and a relative density of 98%, determined from FIB cross-sections such as the one shown in Figure 34.

4.4 Conclusions

This study showed it is possible to produce 98% dense constrained $Ce_{0.9}Gd_{0.1}O_{1.95}$ films at the record low temperature of 950°C on an inert substrate using 3mol% lithium as a dopant. Reducing the strain to full density of the films, and ensuring that a large amount of lithium remained in the film during sintering, were both required to produce dense constrained films at low temperature.

Chapter 5

Summary

5.1 Summary

The results of this work can be summarized as follows. First, using the Vegard's Slope Quality Factor analysis of Chapter 2, an estimate of a sintering aid's effectiveness can be made simply based on a its charge, size, and the high temperature vapor pressure of its oxide. In this manner, two previously unproven CGO sintering aids, lithium and zinc, were identified and evaluated experimentally. Further, since all dilatometry experiments in this thesis were performed on a single batch of CGO powder, the influence of differing CGO particle size distributions was eliminated, allowing a direct comparison of sintering aid effectiveness. This is by far the largest sintering aid study conducted on a single batch of CGO powder to date, and the success of the Vegard's Slope Quality Factor analysis at explaining the observed phenomenon suggests the Vegard's Slope Quality Factor analysis could be applied to other ceramic systems as well. Further, dilatometric and SEM studies on 3mol% Li-CGO showed that CGO could be sintered to full density at 800°C when unconstrained and 950°C when constrained. These are the lowest $Ce_{0.9}Gd_{0.1}O_{1.95}$ sintering temperatures ever achieved, and as suggested by the Vegard's Slope Quality Factor analysis, are probably the lowest that can be achieved. As shown in Chapter 3, the lithium acts to lower the sintering temperature by forming a liquid phase and as shown in Chapter 4, this liquid aids in the densification of constrained films. This is the first time a dense constrained CGO film has been made on an inert substrate. The demonstration that dense, crack-free constrained CGO films can be made from cheap, colloidal methods by directly

introducing the dopant to the constrained layer, instead of relying on dopant migration from the substrate, may prompt those relying on Fe and Mn migration from a steel support to introduce the dopant directly into the electrolyte layer. This would be beneficial because currently these films must be fired in a water rich atmosphere [46] (due to the fact that $Fe(OH)_x$ and $Mn(OH)_x$ are much more mobile in the vapor phase than the base metal or the oxide species) that promotes deleterious chromium migration during firing. In addition, this work showed that reducing the strain to full density and keeping the atmosphere dopant saturated during firing is critical for producing dense constrained films.

In summary, this work has confirmed the hypothesis that dense, crack-free constrained $Ce_{0.9}Gd_{0.1}O_{1.95}$ films can be made at temperatures less than 1000ºC using liquid phase sintering. With some additional work, films manufactured in this way could help commercialize metal supported, ceria based solid oxide fuel cells.

Chapter 6

Future Work

6.1 Post-Sintering Removal of Lithium

6.1.1 INTRODUCTION

As mentioned earlier, the main problem with using sintering aids to lower the sintering temperature of CGO is that they remain at the grain boundaries after sintering and can have the negative effect of inducing electronic conduction or reducing the oxygen ion conductivity. One of the potential benefits of using lithium as a dopant is that its' high vapor pressure in air, approximately ~10^{-9} atm. at 850°C as shown in Figure 21, and the high grain boundary mobility of lithium in CGO, as evidenced by Figure 30, suggests it might be possible to remove it from the CGO after sintering. Post sintering removal of the dopant would help prevent the liquid phase assisted grain coarsening (shown in Figure 22) and the reduction in the oxygen ion conductivity seen in as sintered bulk specimens (shown in Figure 25). In fact, such transient liquid phase sintering of another lithium rich dopant, LiF, has been used since the 1960's to produce dense, transparent MgO [48].

6.1.2 PRELIMINARY EXPERIMENTS

To evaluate the potentially transient nature of the lithium, conductivity tests were prepared on sintered bulk 3mol% Li-CGO samples that were polished flat and had either Au or Pt electrodes, approximately 60nm in thickness, sputtered onto them. These samples were then loaded into a push-contact furnace apparatus and the sample's AC Impedance response was measured from 5 x 10^6 Hz to 0.1Hz using a Solartron 1260 Impedance/Gain

Phase Analyzer after at least 30 minutes of thermal equilibration. The oxygen ion conductivity then determined from the AC Impedance spectrum and the sample's dimensions.

6.1.3 PRELIMINARY RESULTS

Conductivity plots for a single 3mol% Li-CGO bulk sample subjected to a variety of lithium removal schemes is shown in Figure 35. Initially, the bulk electrolyte sample was fired to 1400°C for 4 hours in air inside the dilatometer. After conductivity testing, the Au electrodes were sanded off and the 0.65 g sample was surrounded by 15g of pure CGO powder and fired again for 32 hours at 1200°C in a clean, sealed alumina crucible in the hope that the Li would migrate through the vapor phase to either the alumina crucible walls or the grain boundary regions of the surrounding pure CGO powder. After further conductivity testing and the subsequent removal of the electrodes, the sample was surrounded by 5 g of SiO_2 and fired for 8 hours at 1200°C in a closed alumina crucible in the hope that Li_2SiO_3 would form and pull the lithium out of the sample. Following another conductivity test, not shown in Figure 35, which displayed the same 500°C discontinuity seen previously, the sample was fired for 8 hours at 1200°C in flowing air. When further conductivity testing, not shown in Figure 35, also displayed the 500°C discontinuity, the sample was fired in a vacuum furnace at 3.2×10^{-7} mmHg and 1400°C for 6 hours. Conductivity testing after this vacuum firing, shown in Figure 35, again displayed the 500°C discontinuity.

Throughout these multiple conductivity tests both Au and Pt electrodes were used, but no difference in conductivity behavior was observed. Post conductivity test inspection

of the electrodes often revealed the disappearance of the electrodes where they touched the Pt mesh of the push-contact apparatus, and sometimes revealed a discoloration of the electrodes. The apparent conductivity discontinuity temperature could be raised to as high as 700°C by quickly ramping to high temperature at 10°C/min, suggesting a time activated degradation process. For measurements conducted at the normal ramp rate of 5°C/min, a gradual degradation in the conductivity could be observed at 600°C over the course of 60 minutes, after which a steady-state value was reached. Upon completion of these conductivity tests, a pure CGO reference sample with sputtered Au electrodes was analyzed using the same furnace push-contact apparatus and yielded conductivities in line with the literature values and previous tests.

To evaluate whether the lithium might be removed given the higher surface to volume ratio of a Li-CGO film (compared to that of a bulk sample), an unpressed 3mol% Li-CGO film on a pure CGO substrate was fired for 4 hours at 1100°C in a atmosphere unsaturated with lithium. Unfortunately, the conductivity analysis, shown in Figure 36, showed behavior similar to that seen for the bulk electrolyte sample.

6.1.4 PRELIMINARY DISCUSSION

There is multiple evidence suggesting that, at least to some extent, the lithium in Li-CGO is transient. First, many 3mol% Li-CGO bulk samples fired to 800°C had regions that could not be polished smooth, presumably because of mechanically weak, lithium-rich, intergranular films. In contrast, 3mol% Li-CGO bulk samples fired to 1400°C could be polished smooth and thermally etched without complications, as shown in Figure 27. Further, while it was easy to find intergranular films in 3mol% Li-CGO bulk samples fired to 800°C inside the TEM, such films were much more rare in 3mol% Li-CGO bulk

samples fired to 1400°C. Lastly, only films sintered in a lithium-saturated atmosphere densified, suggesting a loss of lithium at elevated temperature.

At the same time, the post-sintering conductivity analyzes presented here suggest that the lithium rich intergranular films observed in Figure 30 cannot be fully removed through the vapor phase at high temperature. Since it is not observed with the pure material under the same test conditions, the 500°C discontinuity drop must be due to the lithium dopant. The fact that the conductivity remains dreadfully low upon retesting when using the original electrodes, but returns to it's initial value when the original electrodes are replaced by new ones, suggests this discontinuity results from an electrode reaction or the collection of insulating phase at the electrode. Of these two possibilities, the inert nature of Au and Pt and the independent observation that lithium-rich liquids can extrude from a 3mol% Li-CGO sample (see Chapter 3 for more information) suggests the discontinuity is the result of an ionically insulating liquid forming at the electrode-electrolyte interface.

Unfortunately, while some of the lithium may indeed be transient, it is not possible to remove all of the lithium by vaporization within a reasonable amount of time simply by heat-treating. It may be that an intergranular, lithium rich liquid phase becomes thermodynamically stable because it helps separate the negative space-charge layers of the adjacent grains.

6.1.5 POTENTIAL FUTURE EXPERIMENTS

The inability to remove lithium via the vapor phase suggests that other techniques must be employed. Thankfully, the fact that the lithium can be drawn to the ceramic-metal interface suggests that the lithium can be removed by physically driving the liquid out from between the grains by adjusting the surface tension.

Simply hot-pressing 3mol% Li-CGO would be a quick and easy way to determine if the lithium could be removed from the grain boundaries. Indeed, in the classic LiF-MgO transient liquid phase sintering system, one must hot-press the material to remove the LiF liquid [48]. Of course, from a manufacturing point of view hot-pressing is not desirable. One way to pressurize a constrained CGO film in a manufacturing setting would be to employ a metal substrate with a higher thermal expansion coefficient than the CGO electrolyte. The CGO could then be densified at 950C and then annealed at to some lower temperature to drive off the lithium.

Another option for driving off the lithium would be to anneal the film in a slightly reducing atmosphere. Upon reduction from the 4+ to 3+ oxidation state, ceria expands and the added stress could help expel the liquid, provided it didn't crack the film. Additionally, firing in a reducing atmosphere could alter the CGO surface tension and make it more favorable for the liquid to spread across the film surface as seen for the case of magnesia partially stabilized zirconia [42]. Whatever the method, it is clear that the lithium must be removed after sintering if the constrained CGO films developed in this work are going to be useful for SOFC applications.

6.2 Explaining the Lithium Salt Effect

One of the most intriguing outcomes of this work is the dependence of the sintering temperature on the type of dopant salt. Figure 24 shows the effect of three families of lithium salts on the sintering of $Ce_{0.9}Gd_{0.1}O_{1.95}$: those that decompose to Li_2O at elevated temperature ($LiNO_3$, $LiC_2H_3O_2$, $LiOH$, Li_2CO_3, Li_2SO_4), those that are metastable even at room temperature (LiI, $LiBr$), and those that are stable in air at all encountered temperatures ($LiCl$, LiF, $Li_2B_4O_7$, LiH_2PO_4). The direct relation between the

decomposition temperature and the maximum strain rate temperature shown in Figure 37, suggests that sintering begins as soon as Li_2O appears.

One way to test this hypothesis would be to decompose some high decomposition temperature lithium salts (such as lithium carbonate) at low temperature in a vacuum furnace and then analyze these powders in a dilatometer to see if the sintering curves were modified. Unfortunately, attempts to conduct this experiment have been thwarted by the kinetic limitations of decomposing lithium carbonate and lithium sulfate in a 10^{-9} atmosphere at 600°C.

6.3 Production of a Metal Supported Fuel Cell

Provided the lithium can be removed from the film after sintering, there is a very good chance lithium doped CGO could be used for SOFC applications. It is envisioned that to make a metal supported Li-CGO solid oxide fuel cell, a NiO-CGO anode and then a 3mol%Li-CGO electrolyte will be colloidally sprayed atop a porous, prefabricated stainless steel interconnect. This composite will then be fired in a slightly reducing, lithium saturated atmosphere ($pO_2=10^{-12}$) at 950°C so that the steel is not excessively oxidized, the NiO decomposes to metallic nickel (to provide an interconnected electronic pathway in the anode), and the Li-CGO sinters to full density. The use of a Ni-CGO anode has the added benefit that the decomposition of the NiO should locally raise the pO_2 from what the nearby stainless steel would like it to be ($pO_2=10^{-24}$ at 950°C). This should help protect the CGO from the widespread reduction of Ce^{4+} to Ce^{3+} that occurs at pO_2 levels below 10^{-14} at 950°C and tends to crack the film. After this "high temperature" fire, the lithium could be removed, the cathode layer applied, the cells stacked, and the assembly fired near 750°C

to neck together the cathode particles. Such a cheap, colloidally based synthesis route, made possible by the Li-CGO electrolyte, could dramatically lower the cost and increase the long term performance of solid oxide fuel cells.

Appendix I

Derivation of the Reduced Densities and Densification Rates

of Constrained Films
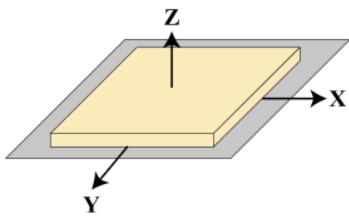
Scherer and Garino [43] developed much of the theory on the constrained sintering of viscous films, which is assumed to also apply for the films comprised of solid particles surrounded by liquid films studied here. However, in their paper they simply list the beginning and ending equations. In this appendix, the full derivation is presented and discussed. Scherer and Garino assumed that the total strain rate in the z-direction, which is also the normalized densification rate for the film since the film is completely constrained in the x and y directions, could be broken into the component caused by sintering (denoted as the free strain rate) and the component caused by the constraining stress (denoted as the creep strain rate). Put mathematically,

Eqn. 14
$$\left(\frac{\dot{\rho}}{\rho}\right) = \dot{\varepsilon}_{Total_z} = \dot{\varepsilon}_{Free_z \ (Not \ Due \ to \ External \ Stress)} + \dot{\varepsilon}_{Creep_z \ (Due \ to \ External \ Stress)}$$

The creep strain rate can be derived from the constitutive relation for an isotropic body, namely,

Eqn. 15
$$\begin{pmatrix} \sigma_{XX} \\ \sigma_{YY} \\ \sigma_{ZZ} \\ \sigma_{XZ} \\ \sigma_{YZ} \\ \sigma_{XY} \end{pmatrix} = \begin{pmatrix} \lambda + 2\mu & \lambda & \lambda & 0 & 0 & 0 \\ \lambda & \lambda + 2\mu & \lambda & 0 & 0 & 0 \\ \lambda & \lambda & \lambda + 2\mu & 0 & 0 & 0 \\ 0 & 0 & 0 & 2\mu & 0 & 0 \\ 0 & 0 & 0 & 0 & 2\mu & 0 \\ 0 & 0 & 0 & 0 & 0 & 2\mu \end{pmatrix} \begin{pmatrix} \dot{\epsilon}_{XX} \\ \dot{\epsilon}_{YY} \\ \dot{\epsilon}_{ZZ} \\ \dot{\epsilon}_{XZ} \\ \dot{\epsilon}_{YZ} \\ \dot{\epsilon}_{XY} \end{pmatrix}$$

Inverting this matrix yields,

Eqn. 16
$$
\begin{pmatrix} \dot{e}_{XX} \\ \dot{e}_{YY} \\ \dot{e}_{ZZ} \\ \dot{e}_{XZ} \\ \dot{e}_{YZ} \\ \dot{e}_{XY} \end{pmatrix} =
\begin{pmatrix}
\dfrac{\lambda+\mu}{3\lambda\mu+2\mu^2} & \dfrac{\lambda}{-6\lambda\mu-4\mu^2} & \dfrac{\lambda}{-6\lambda\mu-4\mu^2} & 0 & 0 & 0 \\
\dfrac{\lambda}{-6\lambda\mu-4\mu^2} & \dfrac{\lambda+\mu}{3\lambda\mu+2\mu^2} & \dfrac{\lambda}{-6\lambda\mu-4\mu^2} & 0 & 0 & 0 \\
\dfrac{\lambda}{-6\lambda\mu-4\mu^2} & \dfrac{\lambda}{-6\lambda\mu-4\mu^2} & \dfrac{\lambda+\mu}{3\lambda\mu+2\mu^2} & 0 & 0 & 0 \\
0 & 0 & 0 & \dfrac{1}{2\mu} & 0 & 0 \\
0 & 0 & 0 & 0 & \dfrac{1}{2\mu} & 0 \\
0 & 0 & 0 & 0 & 0 & \dfrac{1}{2\mu}
\end{pmatrix}
\begin{pmatrix} \sigma_{XX} \\ \sigma_{YY} \\ \sigma_{ZZ} \\ \sigma_{XZ} \\ \sigma_{YZ} \\ \sigma_{XY} \end{pmatrix}
$$

Due to the thin nature of the film in the z-direction, and the fact that there are no principle stresses in this direction, the film is in a plane stress situation where:

Eqn. 17
$$\sigma_{XZ} = \sigma_{YZ} = \sigma_{ZZ} = 0$$

Thus, the matrix can be rewritten as

Eqn. 18
$$
\begin{pmatrix} \dot{e}_{XX} \\ \dot{e}_{YY} \\ \dot{e}_{ZZ} \\ \dot{e}_{XZ} \\ \dot{e}_{YZ} \\ \dot{e}_{XY} \end{pmatrix} =
\begin{pmatrix}
\dfrac{\lambda+\mu}{3\lambda\mu+2\mu^2} & \dfrac{\lambda}{-6\lambda\mu-4\mu^2} & \dfrac{\lambda}{-6\lambda\mu-4\mu^2} & 0 & 0 & 0 \\
\dfrac{\lambda}{-6\lambda\mu-4\mu^2} & \dfrac{\lambda+\mu}{3\lambda\mu+2\mu^2} & \dfrac{\lambda}{-6\lambda\mu-4\mu^2} & 0 & 0 & 0 \\
\dfrac{\lambda}{-6\lambda\mu-4\mu^2} & \dfrac{\lambda}{-6\lambda\mu-4\mu^2} & \dfrac{\lambda+\mu}{3\lambda\mu+2\mu^2} & 0 & 0 & 0 \\
0 & 0 & 0 & \dfrac{1}{2\mu} & 0 & 0 \\
0 & 0 & 0 & 0 & \dfrac{1}{2\mu} & 0 \\
0 & 0 & 0 & 0 & 0 & \dfrac{1}{2\mu}
\end{pmatrix}
\begin{pmatrix} \sigma_{XX} \\ \sigma_{YY} \\ 0 \\ 0 \\ 0 \\ \sigma_{XY} \end{pmatrix}
$$

Multiplying out the normal strain in the z direction, $\dot{\varepsilon}_{zz}$, using this matrix and plugging this into **Eqn. 14** for the creep strain rate yields

Eqn. 19
$$\dot{\varepsilon}_{\text{Total}_z} = \dot{\varepsilon}_{\text{Free}_z} - \frac{\lambda}{6\lambda\mu+4\mu^2}\sigma_{XX} - \frac{\lambda}{6\lambda\mu+4\mu^2}\sigma_{YY}$$

Noting the symmetry of the stress state, so that

Eqn. 20
$$\sigma_{XX} = \sigma_{YY}$$

And recasting the first and second lame parameters, λ and μ, in terms of two other constants, ν and E, using the equations such that

Eqn. 21
$$\lambda = \frac{E\nu}{(1+\nu)(1-2\nu)}$$

and

Eqn. 22
$$\mu = \frac{E}{2(1+\nu)}$$

One obtains the relation,

Eqn. 23
$$\left(\frac{\dot{\rho}}{\rho}\right) = \dot{\varepsilon}_{Total_Z} = \dot{\varepsilon}_{Free_Z} + \frac{2\nu}{E}\sigma$$

This critical equation reveals the effect an in-plane stress has on the densification rate. For constrained films the stress is tensile, which is negative by definition, and therefore the film densification rate is reduced. E is the viscosity of the film and ν is commonly referred to as the "viscous poisson ratio" due to the fact that it is defined from the lame parameters as it would be if this were an elasticity problem. Unlike an elastic poisson ratio which is related to the directionality and rigidity of a meterial's atomic bonds, the viscous poisson ratio is simply an algebraic agglomeration of the fundamental material constants, although both relate stress in one direction to length changes in another direction.

To put the densification rate in terms of only the "viscous poisson ratio", we must make use of Scherer and Garino's original notion that the strain rate can be broken into its densification and creep components, and the fact that the film is completely constrained in the x/y directions. Mathematically,

Eqn. 24
$$\dot{\varepsilon}_{Total_X} = \dot{\varepsilon}_{Free_X \text{ (Not Due to External Stress)}} + \dot{\varepsilon}_{Creep_X \text{ (Due to External Stress)}} = 0$$

Returning to the matrix in **Eqn. 18** to determine the normal strain in the x direction, $\dot{\varepsilon}_{xx}$, and plugging this into **Eqn. 24**, one obtains,

Eqn. 25
$$\dot{\varepsilon}_{\text{Free}_X} + \frac{\lambda + \mu}{3\lambda\mu + 2\mu^2}\sigma_{XX} - \frac{\lambda}{6\lambda\mu + 4\mu^2}\sigma_{YY} = 0$$

Defining ν and E as before and making use the symmetry of the stress state described in **Eqn. 20**, yields

Eqn. 26
$$\sigma = \left(\frac{-\text{E}}{1-\nu}\right)\dot{\varepsilon}_{\text{Free}_X}$$

Finally, plugging the value for the stress obtained from **Eqn. 26** into **Eqn. 23** yields

Eqn. 27
$$\left(\frac{\dot{\rho}}{\rho}\right) = \dot{\varepsilon}_{\text{Total}_Z}(\rho) = \dot{\varepsilon}_{\text{Free}_Z}(\rho)\left(\frac{1+\nu(\rho)}{1-\nu(\rho)}\right)$$

Appendix II

Relating Density to the Dilatometric Percent Linear Change

Since density is mass over volume, the volume of a cube is $l_x*l_y*l_z$, and assuming the mass doesn't change during sintering, the ratio of the initial density (ρ_o) to the density at a temperature T (ρ_T) can be written as:

Eqn. 28
$$\frac{\rho_o}{\rho_T} = \frac{L_{x_T} L_{y_T} L_{z_T}}{L_{x_o} L_{y_o} L_{z_o}}$$

Since the percent linear change recorded by the dilatometer is defined

Eqn. 29
$$PLC_X = \frac{L_{x_T} - L_{x_o}}{L_{x_o}} \times 100$$

Eqn. 30
$$\frac{L_{x_T}}{L_{x_o}} = 1 + PLC_X \times 0.01$$

Plugging this into **Eqn. 28**,

Eqn. 31
$$\rho_T = \frac{\rho_o}{(1 + PLC_X \times 0.01)(1 + PLC_y \times 0.01)(1 + PLC_z \times 0.01)}$$

Assuming isotropic densification, i.e. $PLC_x = PLC_y = PLC_z$, the density at a given temperature can be determined from a uniaxial dilatometer measurement via the equation:

Eqn. 32
$$\rho_T = \frac{\rho_o}{\left(1 + \frac{PLC}{100}\right)^3}$$

Appendix III

Determining Ionic Conductivity from the AC Impedance
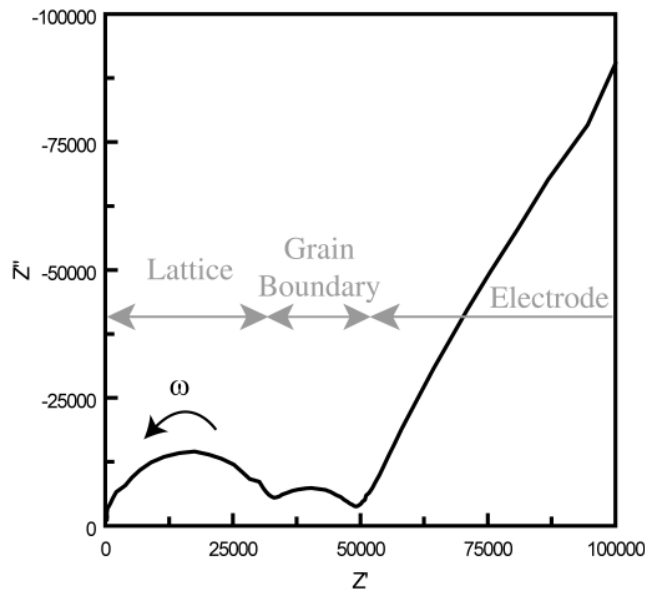
To the left is a representative plot of the real versus imaginary components of the AC Impedance from 1×10^6 Hz to 1 Hz of Pure 90-10 CGO at 200°C. This type of plot is known as a Nyquist plot. The high frequency arc corresponds to ionic conductivity in the lattice, the mid frequency arc corresponds to the ionic conductivity across the grain boundaries and the low frequency arc corresponds to the electrode reaction. These assignments have been made in the literature for ceria by changing the grain size, sample thickness, and electrode material and noting the effect on impedance spectra. Further, it also makes sense conceptually that ionic hops in the lattice occur very quickly (high frequency), while ionic hopping across grain boundaries take a bit longer, and chemical reactions across a dissimilar material interface take the longest.

Each of these processes appears as an arc because each process has a resistive and capacitive component to them that acts in parallel. In terms of impedance (i.e. the relation between the applied AC voltage and the resulting AC current, denoted Z) the response of a resistor is R and the response of a capacitor is 1/jwC where j is the square root of –1, w is

the angular frequency, C is the capacitance, and R is the resistance. Since the resistor and capacitor act in parallel, application of Ohm's law and Kirchhoff's current law yields,

Eqn. 33
$$\frac{1}{Z} = \frac{1}{R} + \frac{1}{1/jwC}$$

Inversion of both sides of the equation yield

Eqn. 34
$$Z = \frac{R}{1 + jwRC}$$

Multiplying top and bottom of the right side by 1-jwRC yields

Eqn. 35
$$Z = \frac{R(1 - jwRC)}{1 + w^2R^2C^2}$$

which can be rewritten as

Eqn. 36
$$Z = \frac{R}{1 + w^2R^2C^2} + j\frac{-wR^2C}{1 + w^2R^2C^2}$$

where the first term is the real part of the impedance (it contains all real terms) and the second term is the imaginary part of the impedance. Thus, for a fixed R and C, a plot of Z as w is varied from 0 to infinity will yield a semicircle on a plot of the Z_{Real} (Z') vs. $Z_{Imaginary}$ (Z"). As can be seen from **Eqn. 36**, when the C=0 Z" equals zero and the impedance equals the resistance. Since the conductivity is the inverse of the resistivity, and the resistivity, ρ, is is defined as:

Eqn. 37
$$\rho = \frac{RA}{l}$$

where A is the cross-sectional area and l is the length, the conductivity of a process can be determined by based on the x-intercepts of the impedance curve and the sample

dimensions. Multiple arcs appear because, as noted earlier, multiple resistive/capacitive processes can act in series. Oftentimes, the range of frequencies at which these different processes are active overlap slightly, with the result that the impedance doesn't actually decrease all the way to the abscissa. Thankfully, in the case of CGO the individual arcs are well resolved and the x-intercepts can be found by fitting the individual arcs.

Tables

Table 1-Vegard's Slopes of All Dopants with Commercially Available Nitrates

Name	8-fold Coordinated Ionic Radius (A	Vegard's Slope (x 100,000)	Previously Studied as a CGO Dopant in Reference:
B^{3+}	0.44*	-131 †	
Si^{4+}	0.54*	-95 †	
Al^{3+}	0.69*	-77	[8]
Ni^{2+}	0.83*	-61	[4, 13]
Ga^{3+}	0.77*	-59	[21]
Mn^{3+}	0.78*	-58 •	[4, 15, 16, 22]
Fe^{3+}	0.78	-57	[4, 11, 13, 15, 17, 18, 20, 47]
Cu^{+}	0.92*	-56 •	
Li^{+}	0.92	-56	
Cu^{2+}	0.89*	-48	[4, 11, 13]
Mg^{2+}	0.89	-48	
Co^{2+}	0.90	-45	[4, 11-15, 23]
Zn^{2+}	0.90	-45	[4, 11, 13]
Fe^{2+}	0.92	-41 •	
Sc^{3+}	0.87	-37	
Mn^{2+}	0.96	-32	
Hf^{4+}	0.83	-31	
Zr^{4+}	0.84	-29	
In^{3+}	0.92	-26	
Lu^{3+}	0.98	-13	
Tl^{3+}	0.98	-13	
Yb^{3+}	0.99	-12	
Tm^{3+}	0.99	-10	
Er^{3+}	1.00	-8	
Pd^{2+}	1.08*	-6	
Ho^{3+}	1.02	-5	

Y^{3+}	1.02	-4	
Dy^{3+}	1.03	-2	
Cd^{2+}	1.10	-1	
Tb^{3+}	1.04	0	
Na^{+}	1.18	1	
Ca^{2+}	1.12	3	
Gd^{3+}	1.05	3	
Eu^{3+}	1.07	6	
Hg^{2+}	1.14	7	
Sm^{3+}	1.08	9	
Nd^{3+}	1.11	16	
Pr^{3+}	1.13	19	
Ce^{3+}	1.14	23	
Ag^{+}	1.28	23	
La^{3+}	1.16	27	[13]
Bi^{3+}	1.17	29	[9]
Sr^{2+}	1.26	34	[13]
Hg^{+}	1.34*	36	
Pb^{2+}	1.29	40	
Ba^{2+}	1.42	69	
K^{+}	1.51	74	
Tl^{+}	1.59	92	
Rb^{+}	1.61	96	
Cs^{+}	1.74	124	

* No 8-fold radii were listed in Shannon's Table [40] for these dopants. Radii were extrapolated from lower

coordinations. All extrapolated dopants had entries for C.N.=6.

† No Commercially available dopant nitrate exists. Included for reference.

• Even though no dopant nitrate is commercially available, Mn3+ was included because Mn(NO3)2

decomposes to Mn2O3, Cu+ was included because CuO can be reduced at high temperatures, and Fe2+

was included because Fe2O3 can be reduced at high temperature.

Highlighted CGO dopants were studied in this thesis.

Table 2- Density of Various Dopant Oxide Phases

Data from Ref. [49]

Phase	Density (g/cm^3)
Fe_2O_3	5.25
Fe_3O_4	5.17
Mn_2O_3	5.0
Mn_3O_4	4.84
CuO	6.31
Cu_2O	6.0

Table 3- Sintered Pellet Conductivities at 200°C

Sample	Log Lattice Conductivity (S/cm)	Log Grain Boundary Conductivity (S/cm)	Log Total Conductivity (S/cm)
Pure CGO	-4.8	-4.5	-5.0
3mol% Al	-4.8	-6.1	-6.1
3mol% Ni	-4.8	-5.5	-5.6
3mol% Li	-4.8	-6.5	-6.5
3mol% Co	-4.8	-4.9	-5.2
3mol% Cu	-4.9	-5.9	-5.9
3mol% Mg	-4.8	-5.1	-5.3
3mol% Fe	-4.9	-5.6	-5.7
3mol% Mn	-4.9	-6.3	-6.3
3mol% Zn	-4.9	-4.8	-5.1
3mol% K	-5.0	-6.4	-6.4
3mol% Ca	-5.5	-6.4	-6.5

Table 4- Strains and Densities for Green and Sintered CGO Pellets

Sample	Green ρ (%)	Sintered ρ (%)	$\varepsilon_{Dilat.}$	$\varepsilon_{Dens.}$	ε_{Creep}	$\frac{\varepsilon_{Dens.}}{\varepsilon_{Dilat.}} \times 100$
Initial Pure	44.5	94.8	-0.29	-0.26	-0.03	90
1mol% Al	45.2	95.2	-0.28	-0.26	-0.02	91
3mol% Al	44.6	93.0	-0.29	-0.26	-0.03	88
5mol% Al	45.9	93.8	-0.28	-0.26	-0.02	92
1mol% Ca	42.6	95.8	-0.29	-0.28	-0.01	97
3mol% Ca	45.6	94.0	-0.27	-0.26	-0.01	95
5mol% Ca	42.2	94.6	-0.31	-0.28	-0.02	92
1mol% Co	44.4	90.6	-0.29	-0.26	-0.03	88
3mol% Co	44.9	91.6	-0.30	-0.26	-0.04	85
5mol% Co	45.1	93.3	-0.30	-0.25	-0.04	86
1mol% Cu	44.0	91.4	-0.32	-0.25	-0.07	79
3mol% Cu	45.4	88.1	-0.29	-0.23	-0.06	81
5mol% Cu	43.2	87.4	-0.31	-0.26	-0.05	84
1mol% Fe	44.2	91.2	-0.31	-0.25	-0.06	81
3mol% Fe	44.6	85.4	-0.25	-0.23	-0.02	91
5mol% Fe	44.9	85.2	-0.28	-0.23	-0.06	80
1mol% Li	43.2	93.8	-0.28	-0.27	-0.01	98
3mol% Li	44.2	96.2	-0.30	-0.27	-0.02	90
5mol% Li	44.7	95.8	-0.27	-0.27	-0.01	98
1mol% Mg	43.8	96.5	-0.30	-0.27	-0.03	92
3mol% Mg	45.7	95.6	-0.29	-0.26	-0.03	91
5mol% Mg	45.2	94.4	-0.28	-0.26	-0.02	92
1mol% Mn	43.8	91.2	-0.30	-0.25	-0.04	85
3mol% Mn	43.5	89.9	-0.29	-0.25	-0.04	86
5mol% Mn	43.2	91.4	-0.28	-0.26	-0.02	93
1mol% Na	42.4	77.8	-0.24	-0.21	-0.02	90
3mol% Na	44.1	92.9	-0.28	-0.26	-0.02	94
5mol% Na	43.83	98.1	-0.27	-0.24	-0.03	88
1mol% Ni	42.5	95.3	-0.30	-0.28	-0.02	94
3mol% Ni	45.9	95.1	-0.28	-0.26	-0.02	92
5mol% Ni	43.8	94.5	-0.30	-0.28	-0.02	94
1mol% Zn	43.7	94.7	-0.31	-0.27	-0.05	84
3mol% Zn	42.2	94.5	-0.31	-0.28	-0.03	90
5mol% Zn	43.1	92.6	-0.32	-0.27	-0.05	85
Final Pure	42.8	94.6	-0.30	-0.27	-0.02	92

Table 5- Dopant Effectiveness Comparison

Dopant	Effect on T_{sinter}	Obeys Vegard's Slope Analysis	Agrees with Literature CGO Sintering Behavior in Ref:	Disagrees with Literature CGO Sintering Behavior i Ref:
Al^{3+}	Raised	Yes	[8]* for 3,5mol%	[8]* for 1mol%
Ca^{2+}	Minor Effect	Yes		[38]†
Co^{2+}	Lowered	Yes	[4]* [11]* [13] [14]* [15]*	
Cu^{2+}	Lowered	Yes	[4]* [11]* [13]	
Fe^{3+}	Lowered	Yes	[4]* [11]* [13] [47]* [18]* [20]*	
K^{+}	Raised	Yes		
Li^{+}	Lowered	Yes	[50]†	
Mg^{2+}	Minor Effect	No		[38]†
Mn^{2+}	Lowered	Yes	[4]* [16]† [15]*	
Ni^{2+}	Minor Effect	Yes	[13]	[4]*
Zn^{2+}	Lowered	Yes		

† Study performed on pure ceria.   *Study performed on $Ce_{0.8}Gd_{0.2}O_{1.9}$

Table 6- Strain Data for CGO Doped with Various Amounts of Lithium Salts

Dopant	$\varepsilon_{Dilat..}$	$\varepsilon_{Dens.}$	ε_{Creep}	$\dfrac{\varepsilon_{Dens.}}{\varepsilon_{Dilat.}} \times 100$
Pure	-0.29	-0.26	-0.03	90
1mol% Li	-0.28	-0.27	-0.01	98
2mol% Li	-0.30	-0.29	-0.01	98
3mol% Li	-0.30	-0.27	-0.03	90
4mol% Li	-0.26	-0.25	-0.01	98
5mol% Li	-0.27	-0.27	-0.01	98
5mol% Li	-0.27	-0.27	-0.01	98
15mol% Li	-0.30	-0.23	-0.07	77

Table 7- Strain Data for CGO Doped with Various Lithium Salts at the 3mol% Level

Dopant	$\varepsilon_{Dilat..}$	$\varepsilon_{Dens.}$	ε_{Creep}	$\frac{\varepsilon_{Dens.}}{\varepsilon_{Dilat.}} \times 100$
None	-0.29	-0.26	-0.03	90
LiNO$_3$	-0.29	-0.27	-0.02	94
LiOH	-0.29	-0.28	-0.02	95
Li$_2$CO$_3$	-0.29	-0.28	-0.01	96
Li$_2$SO$_4$	-0.23	-0.21	-0.02	91
LiC$_2$H$_3$O$_3$	-0.31	-0.28	-0.02	92
LiI	-0.31	-0.26	-0.05	84
LiBr	-0.29	-0.27	-0.02	93
LiCl	-0.28	-0.25	-0.03	89
LiF	-0.37	-0.27	-0.10	74
LiH$_2$PO$_4$	-0.32	-0.27	-0.05	85
Li$_2$B$_4$O$_7$	-0.34	-0.27	-0.07	80

Figures

Figure 1- Cross Section a Traditional YSZ Fuel Cell

This figure shows traditional material selections, the desired microstructure, and the localized fuel reactions. $La_{0.85}Sr_{0.15}MnO_3$ (LSM) is the traditional cathode material, while a nickel/yttria stabilized zirconia composite is the traditional anode material. Figure modified from Ref. [51].
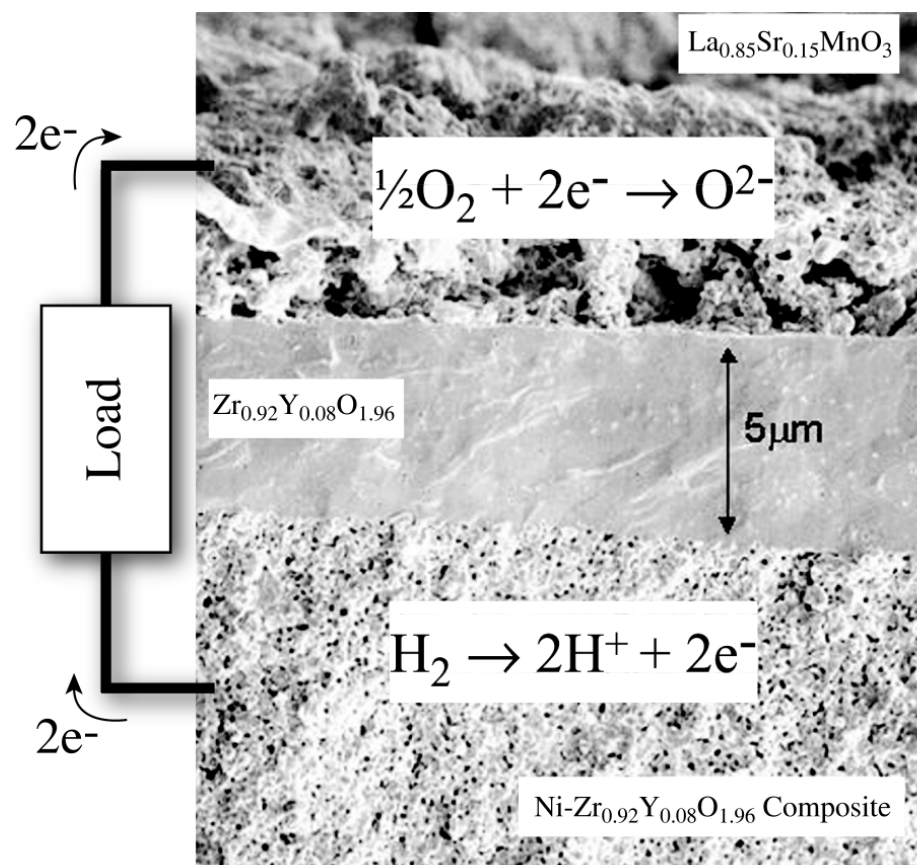
Figure 2- Total Ionic Conductivity of Various SOFC Electrolyte Materials

From Ref. [6].
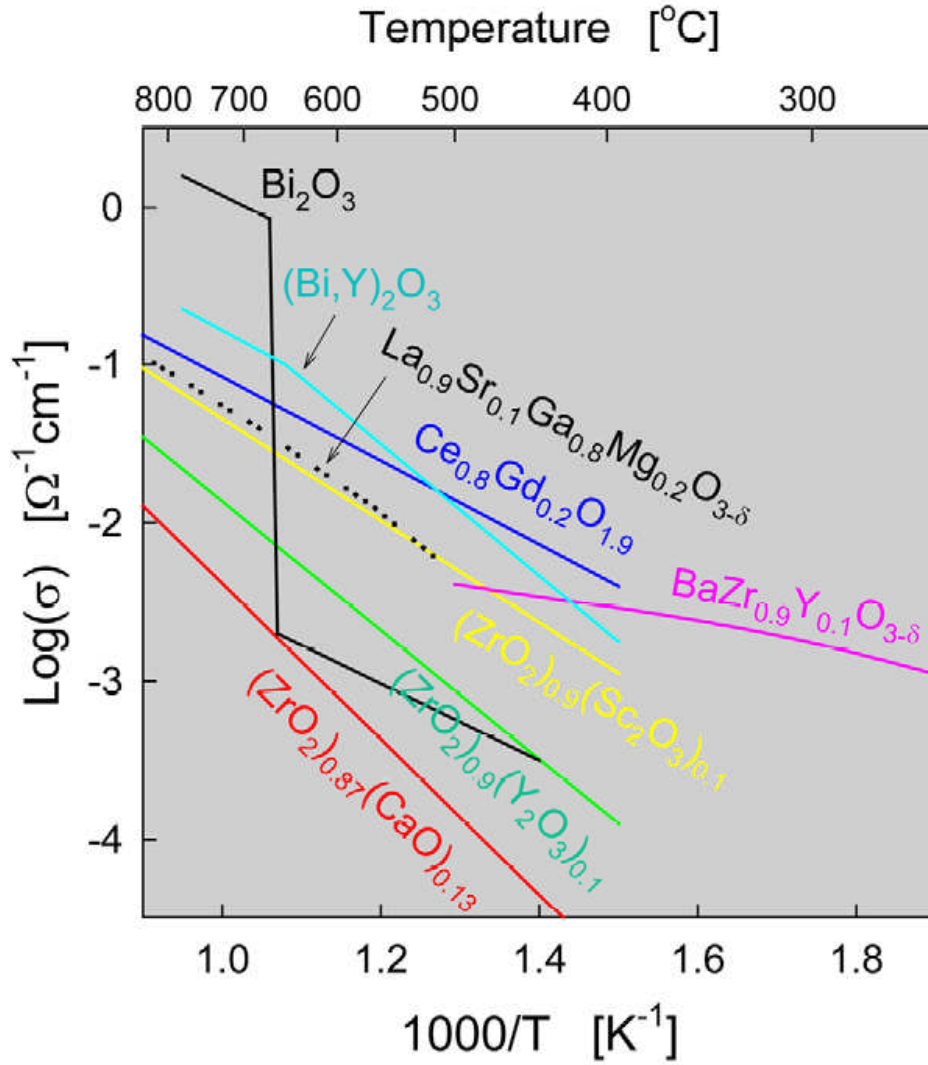
Figure 3- Plot showing the Fit for Kim's Vegard's Slope Equation

From Ref. [26]

$$\Delta a = \sum_i (0.0220 r_i + 0.00015 z_i) m_i$$
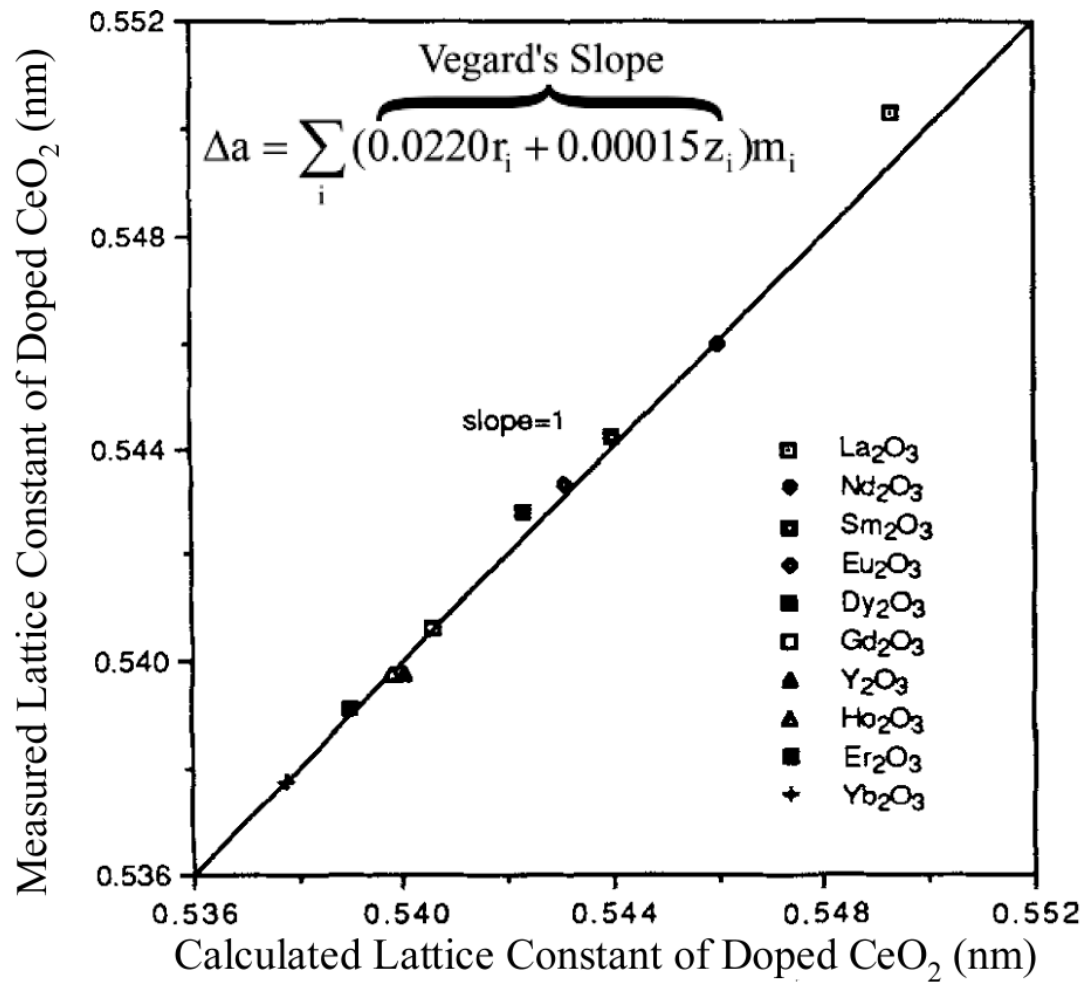
Figure 4- Relationship between Dopant Solubility and Vegard's Slope

Data from Ref [28]
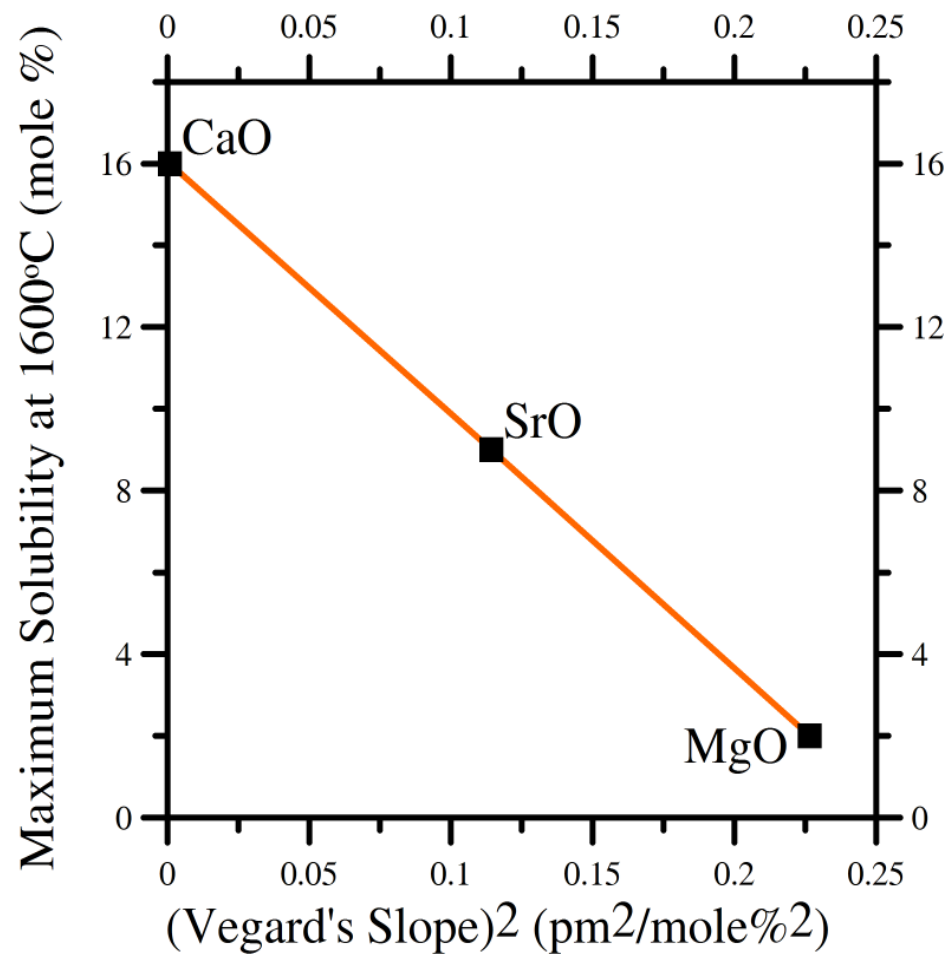
Figure 5- Cation Migration Paths in CGO

From Ref. [31]
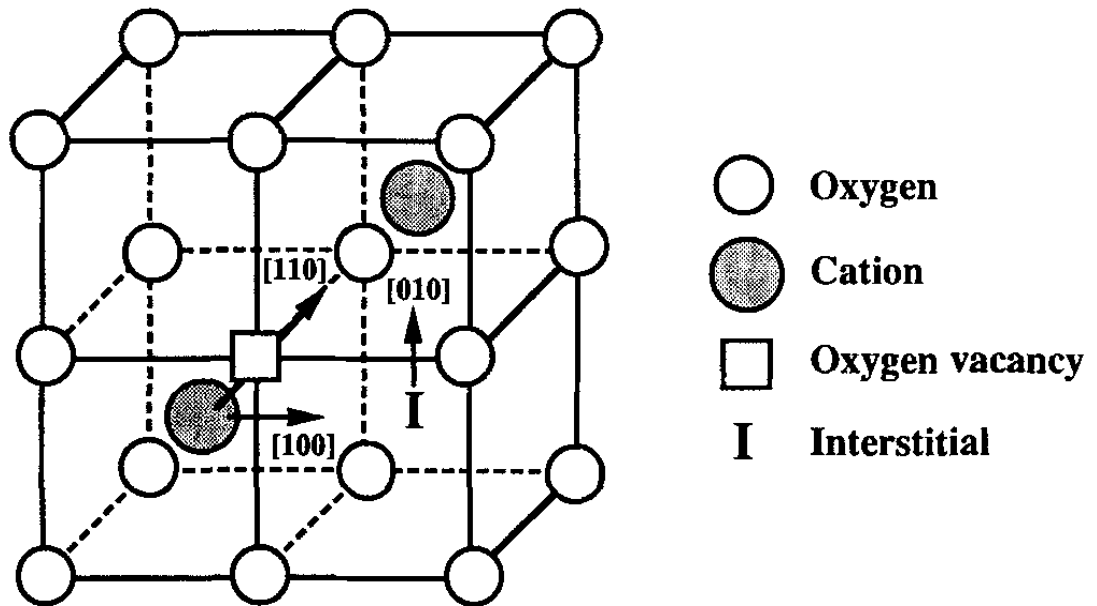
Figure 6- Transmission Electron Micrographs of As-received Ce$_{0.9}$Gd$_{0.1}$O$_{1.95}$ Powder
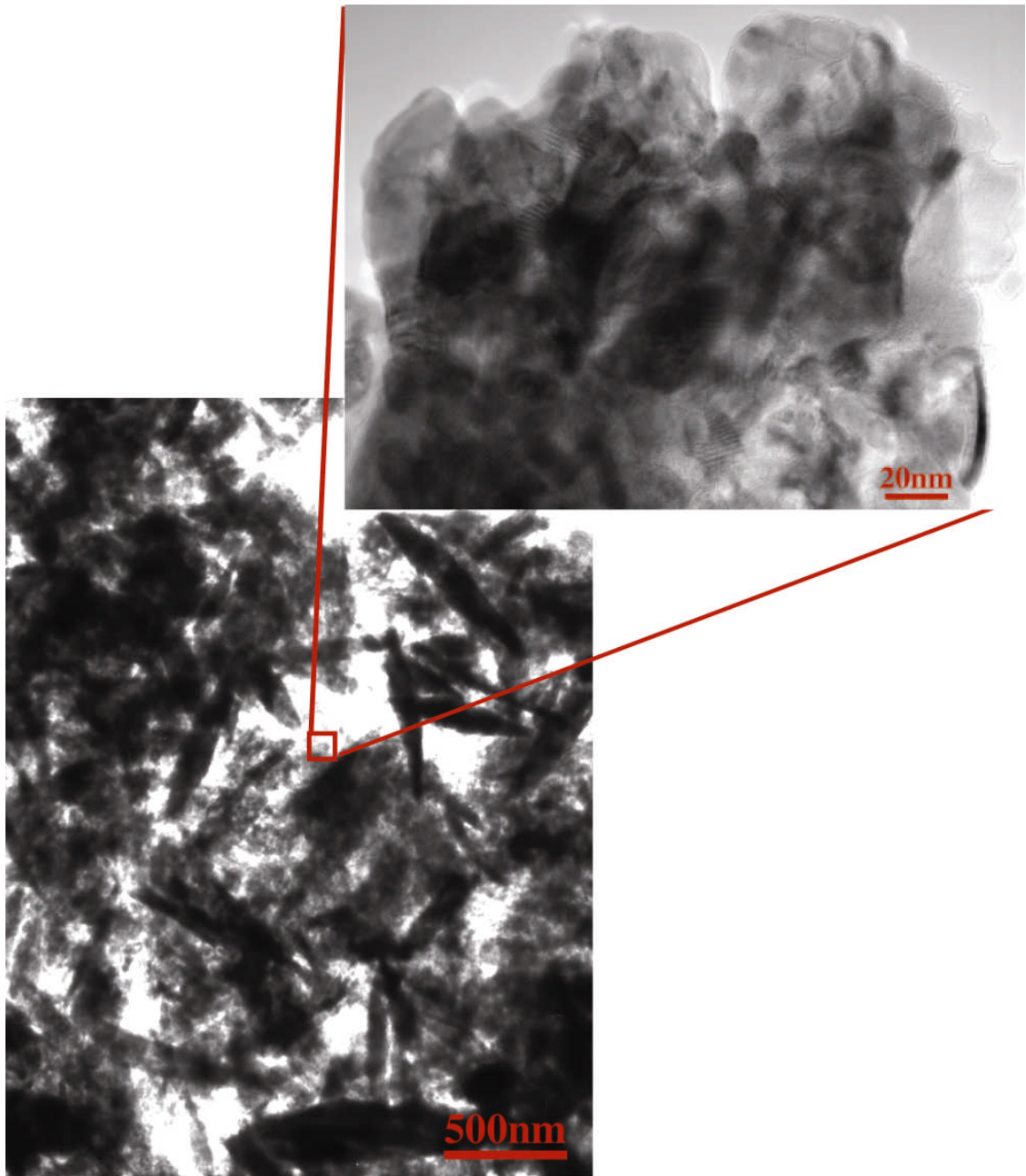
Figure 7- $Ce_{0.9}Gd_{0.1}O_{1.95}$ Doped at the 1mol% Level with Various Dopants
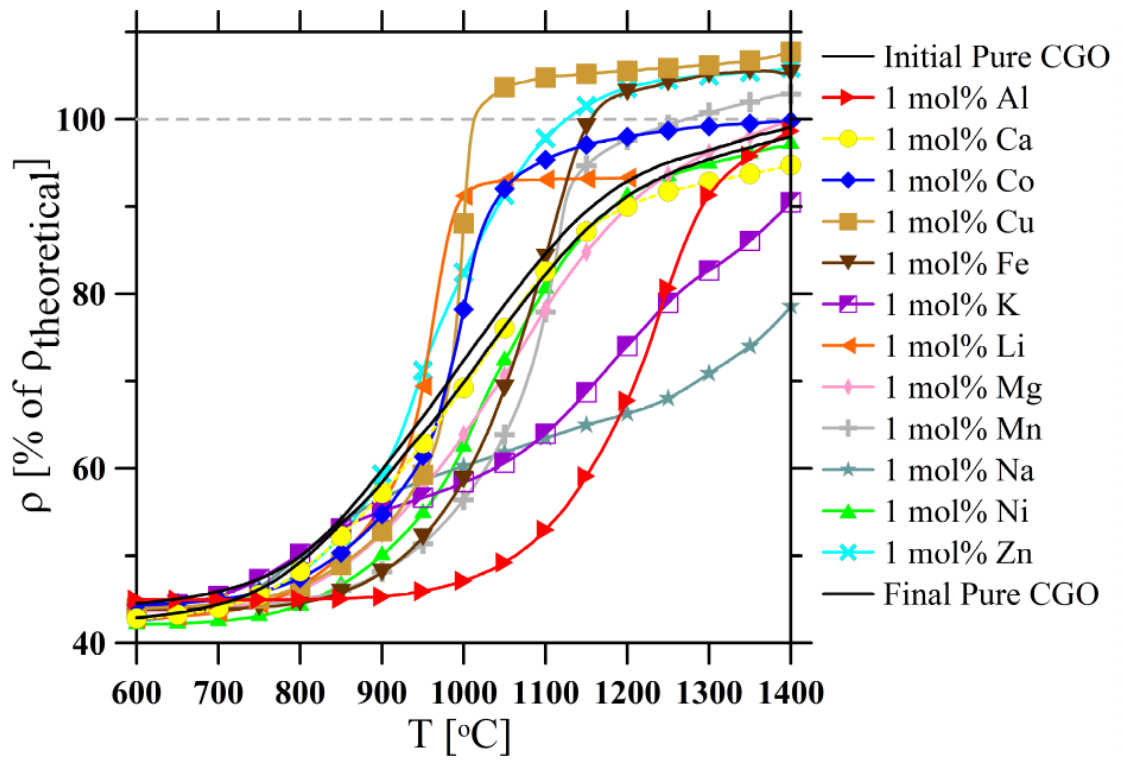
Figure 8- Ce$_{0.9}$Gd$_{0.1}$O$_{1.95}$ Doped at the 3mol% Level with Various Dopants
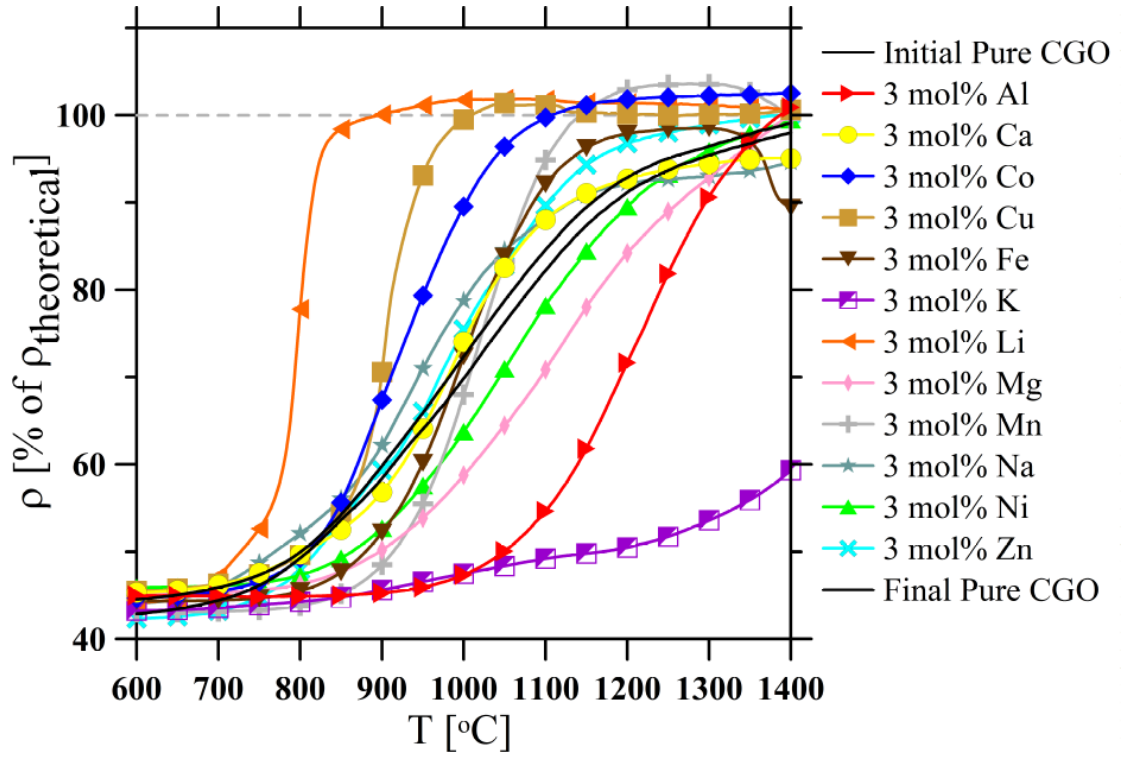
Figure 9- Ce$_{0.9}$Gd$_{0.1}$O$_{1.95}$ Doped at the 5mol% Level with Various Dopants
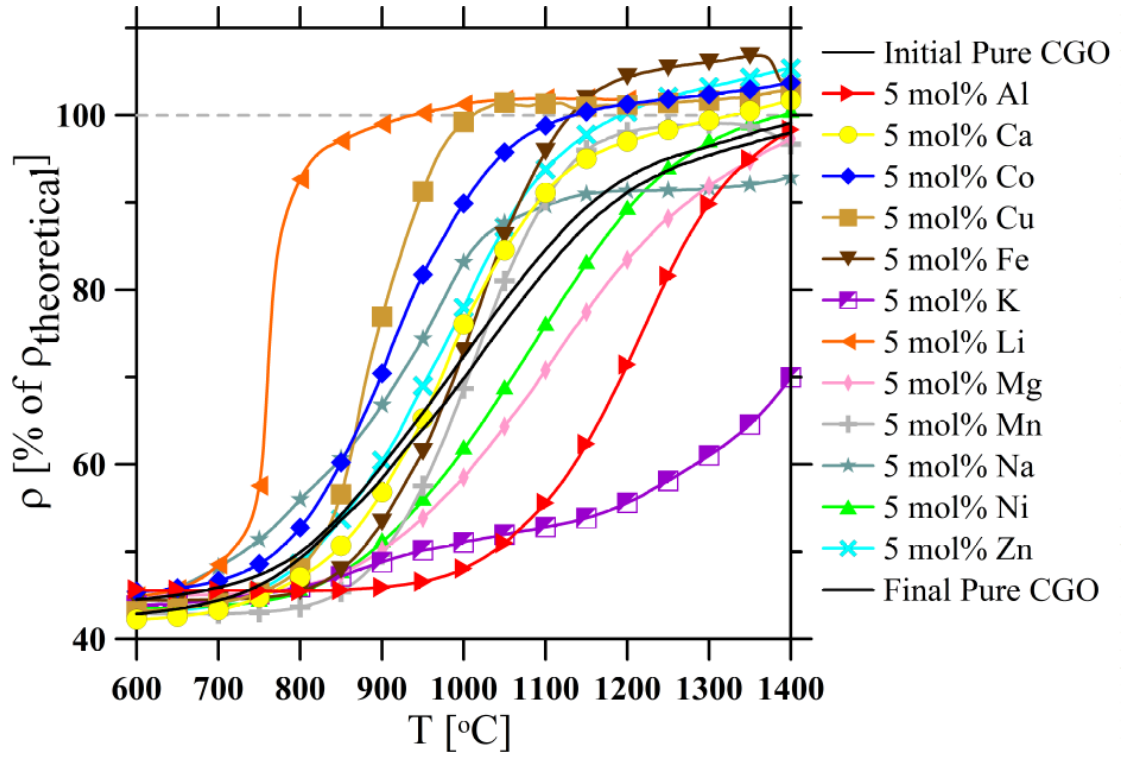
Figure 10- $Ce_{0.9}Gd_{0.1}O_{1.95}$ Doped with Aluminum
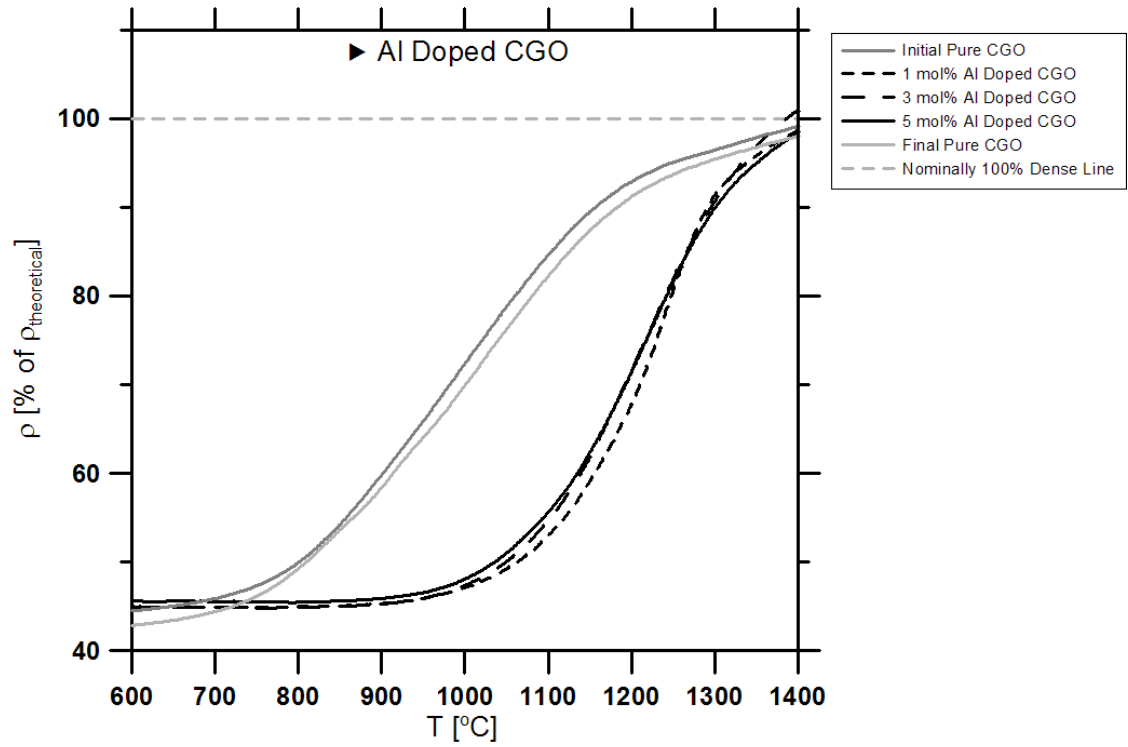
Figure 11- Ce$_{0.9}$Gd$_{0.1}$O$_{1.95}$ Doped with Calcium
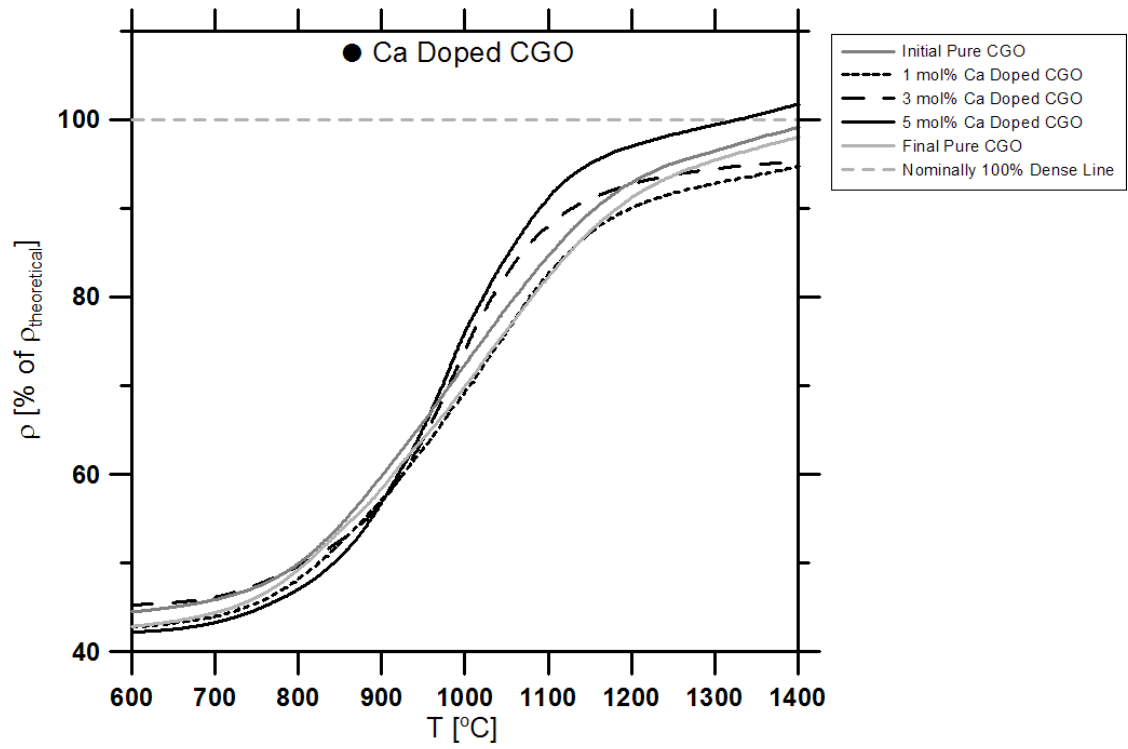
Figure 12- Ce$_{0.9}$Gd$_{0.1}$O$_{1.95}$ Doped with Cobalt
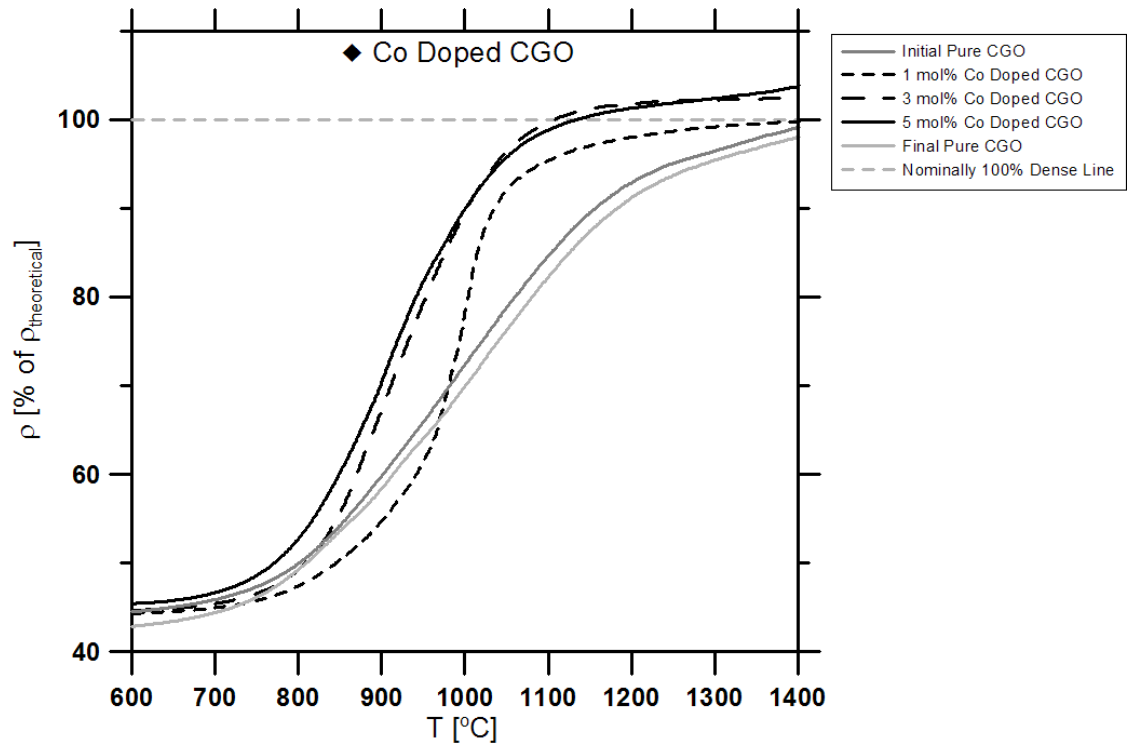
Figure 13- Ce$_{0.9}$Gd$_{0.1}$O$_{1.95}$ Doped with Copper
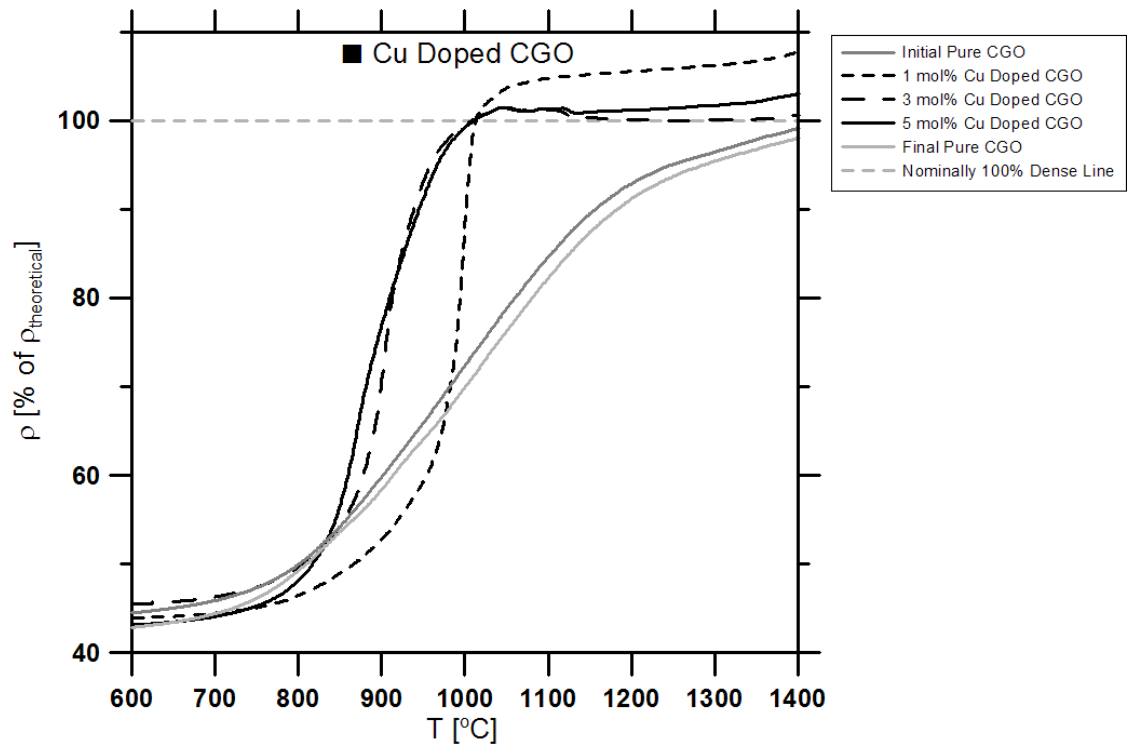
Figure 14- Ce$_{0.9}$Gd$_{0.1}$O$_{1.95}$ Doped with Iron
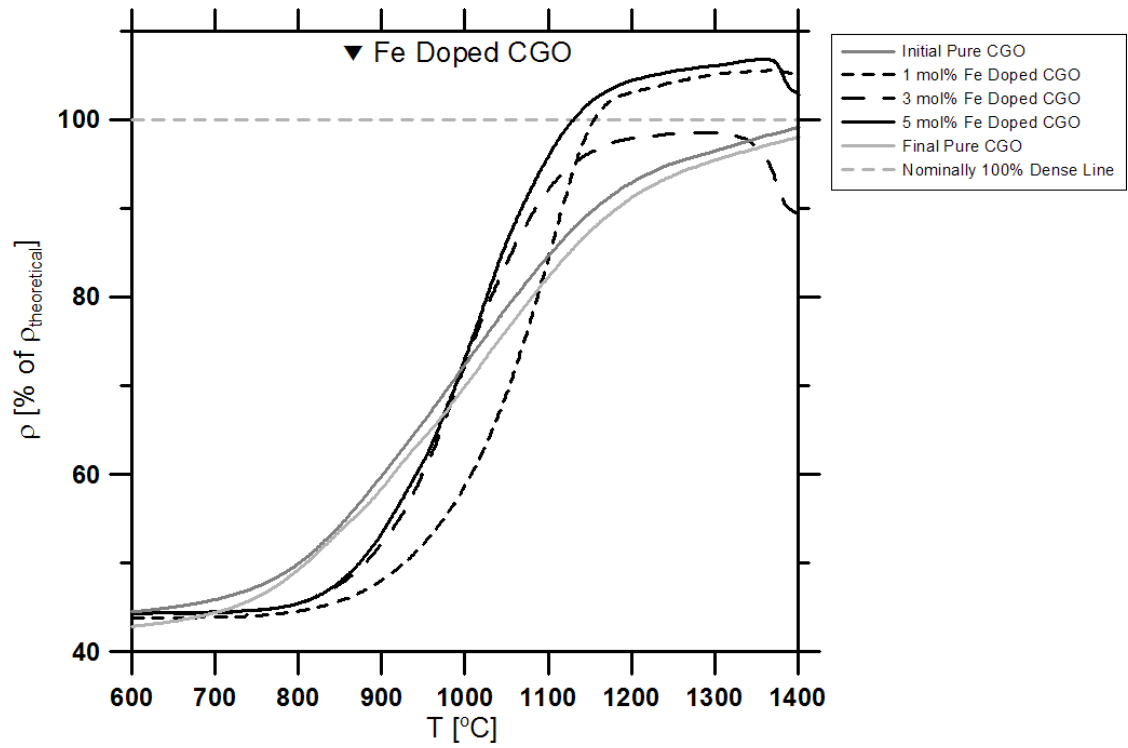
Figure 15- $Ce_{0.9}Gd_{0.1}O_{1.95}$ Doped with Potassium
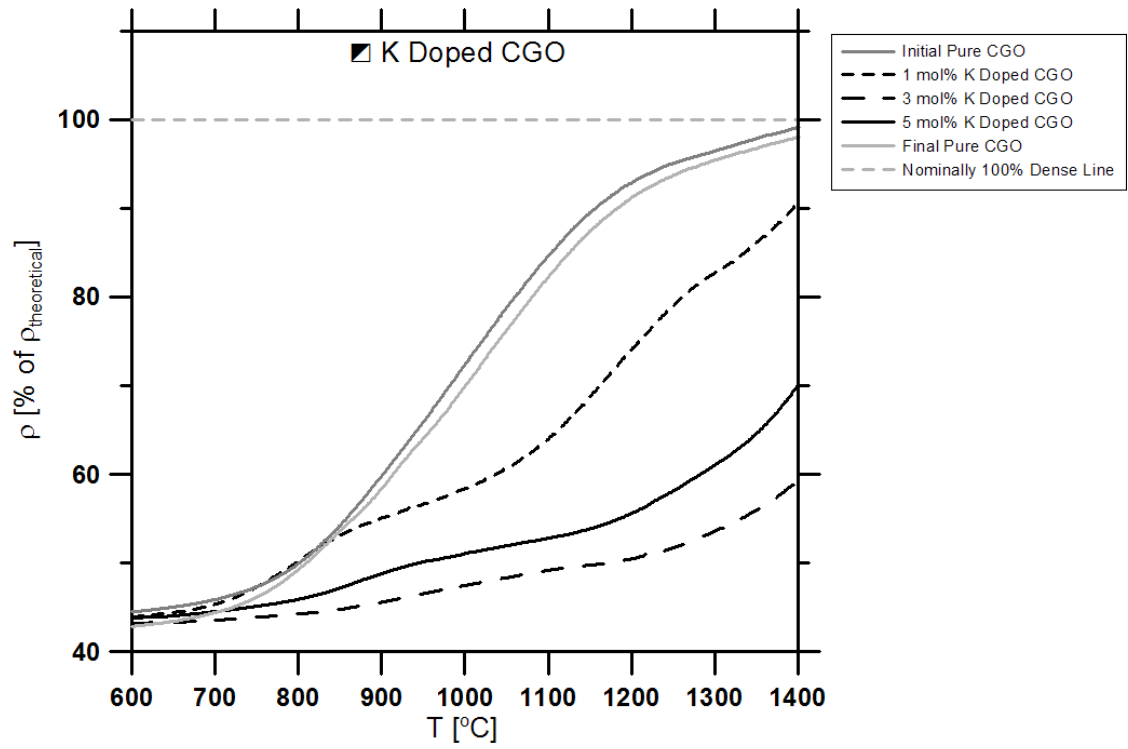
Figure 16- $Ce_{0.9}Gd_{0.1}O_{1.95}$ Doped with Lithium
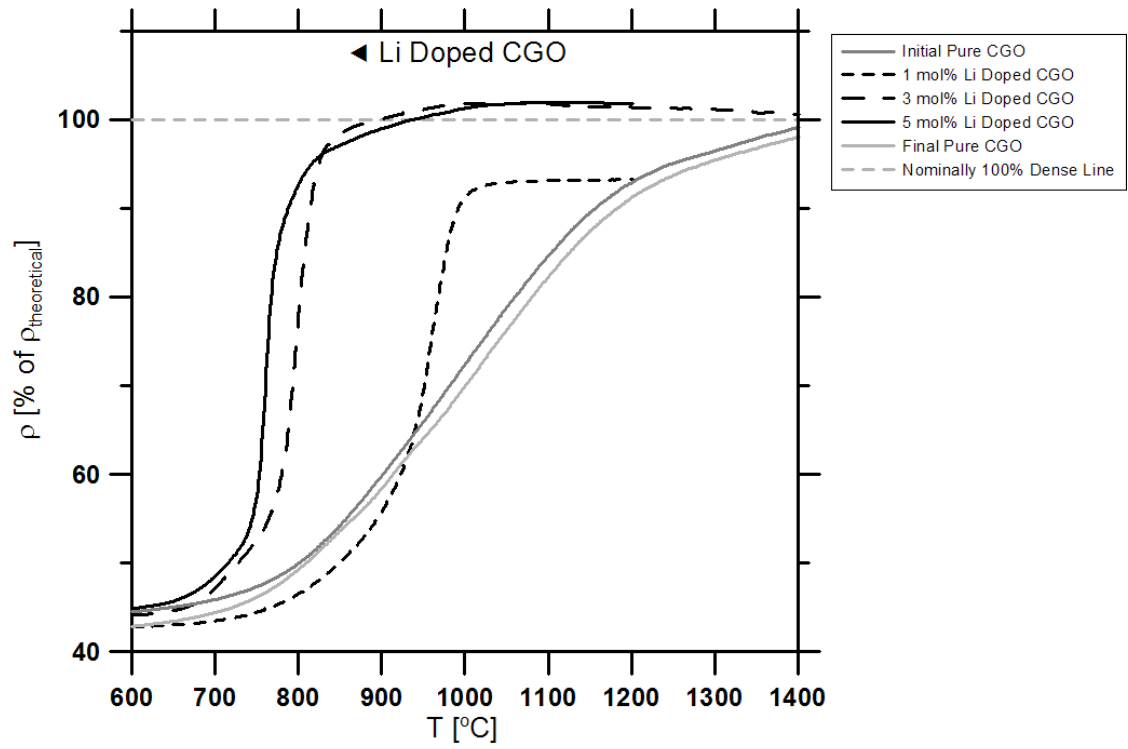
Figure 17- Ce$_{0.9}$Gd$_{0.1}$O$_{1.95}$ Doped with Magnesium
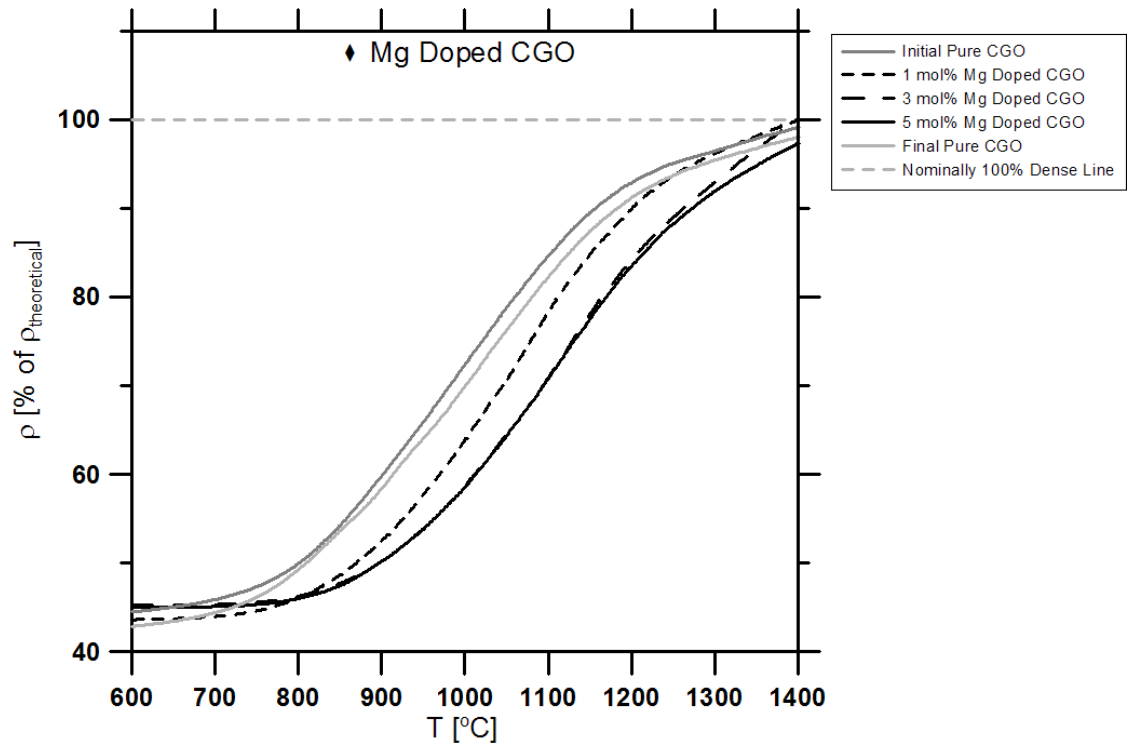
Figure 18- $Ce_{0.9}Gd_{0.1}O_{1.95}$ Doped with Manganese
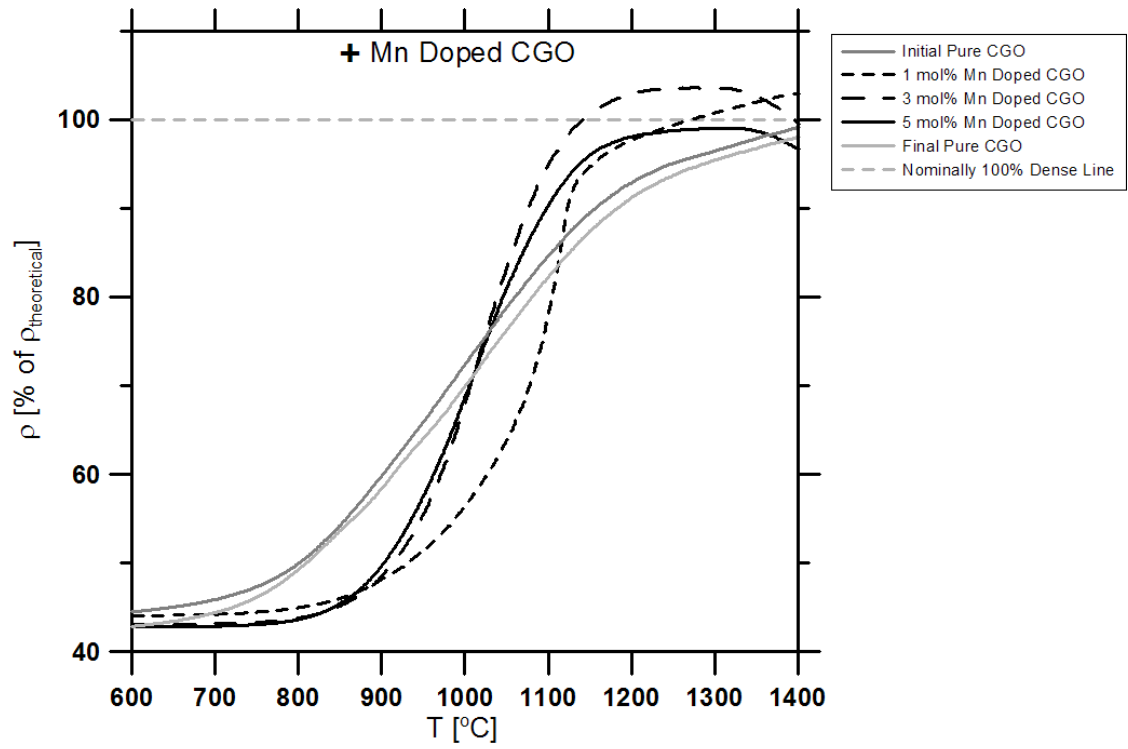
Figure 19- Ce$_{0.9}$Gd$_{0.1}$O$_{1.95}$ Doped with Nickel
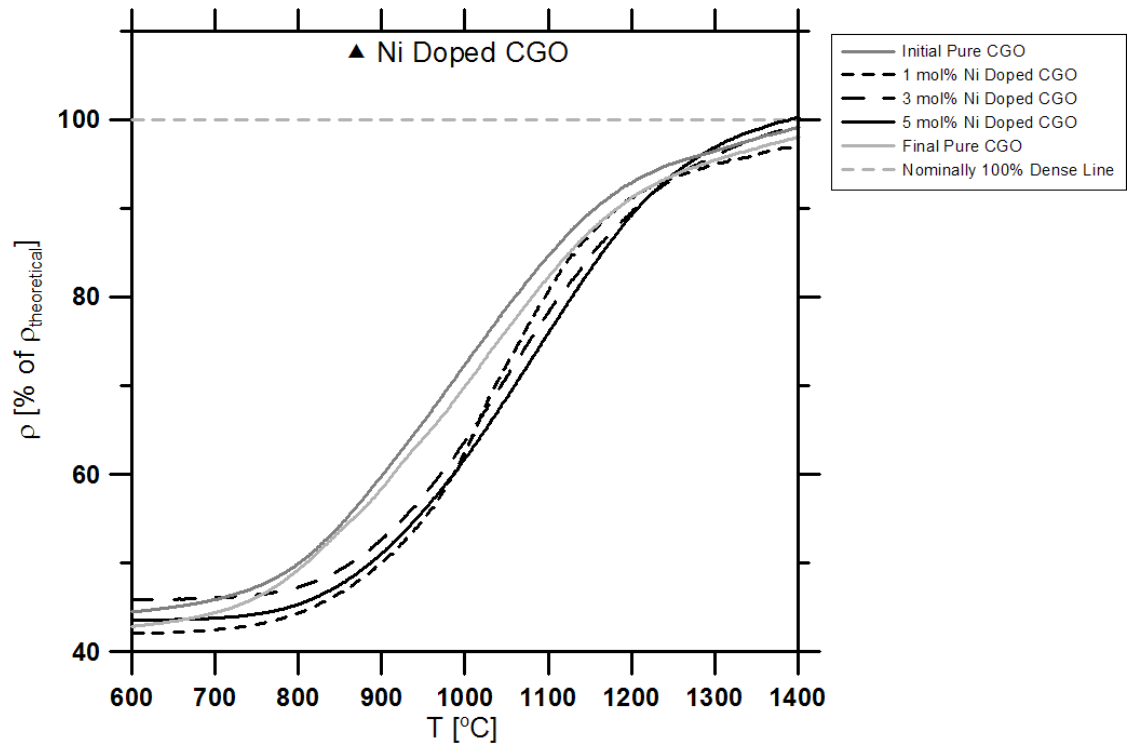
Figure 20- Ce$_{0.9}$Gd$_{0.1}$O$_{1.95}$ Doped with Zinc
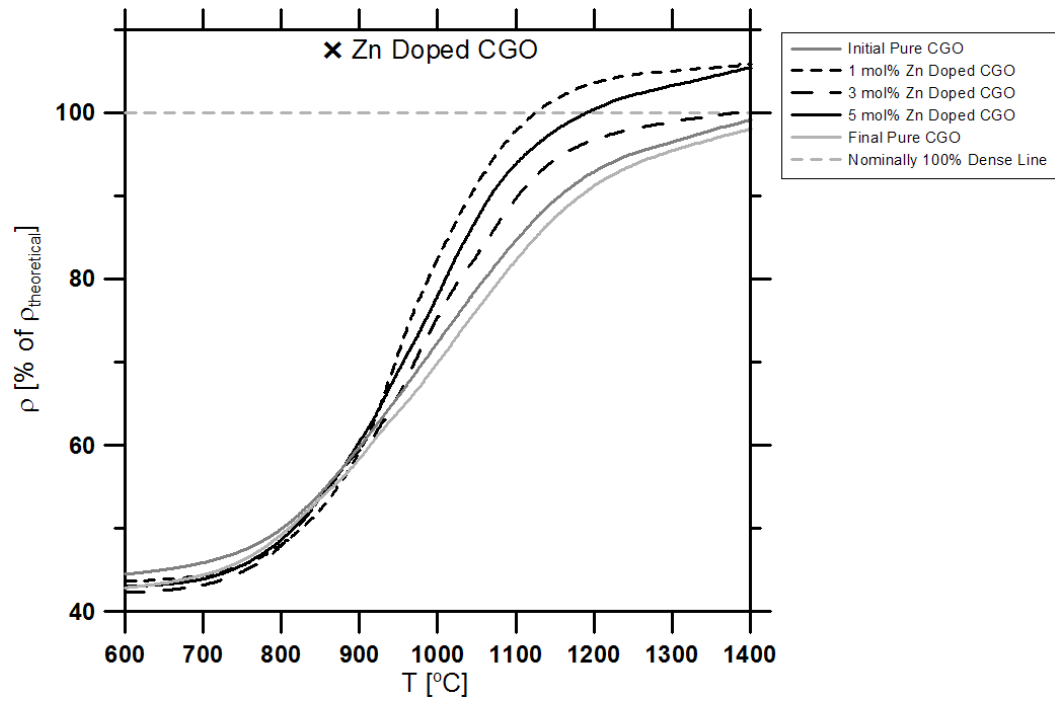
Figure 21- Dopant Volatility vs. Temperature

Data for Al2O3, MgO, ZnO and CaO were taken from Ref. [52]**. Data for Li and KO2 were taken from Ref.** [53]**. Data for CuO was taken from Ref.** [54]**. Data for CoO was taken from Ref.** [55]**. Data for NiO was taken from Ref.** [56]**. Data for FeO was taken from** [57]**. After Brewer and Mastick,**[58] **the data for MnO was obtained from the experimental vapor pressure measurment in Ref.** [58] **and by assuming the same free energy vs. temperature behavior for MnO as for NiO**.
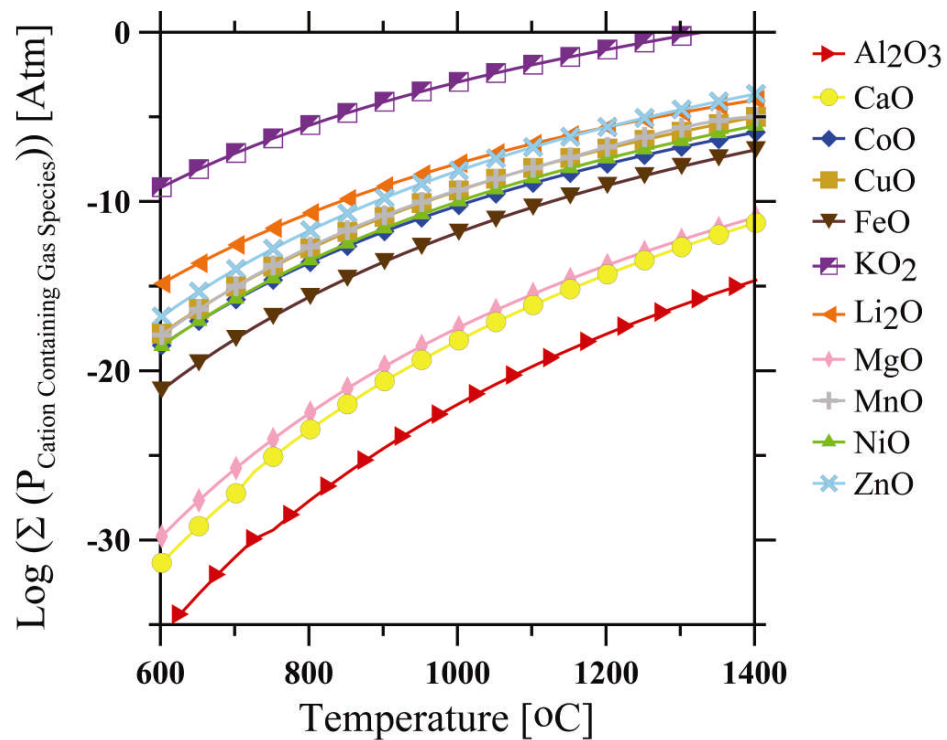
Figure 22- Sintered Doped CGO Grain Sizes
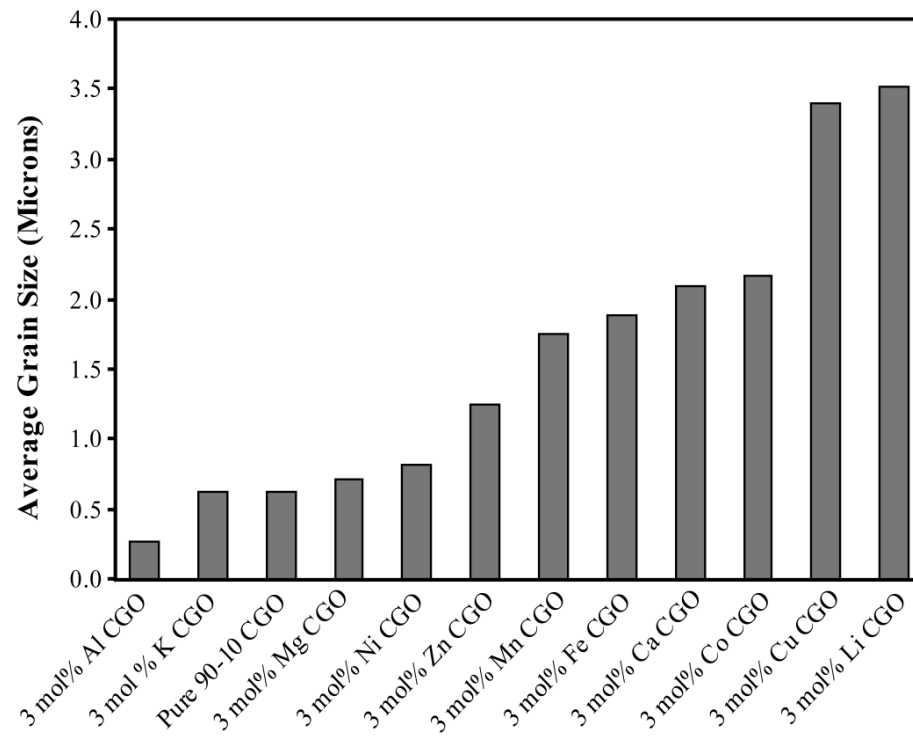
Figure 23- Dilatometry of CGO Doped with Varying Amounts of LiNO₃
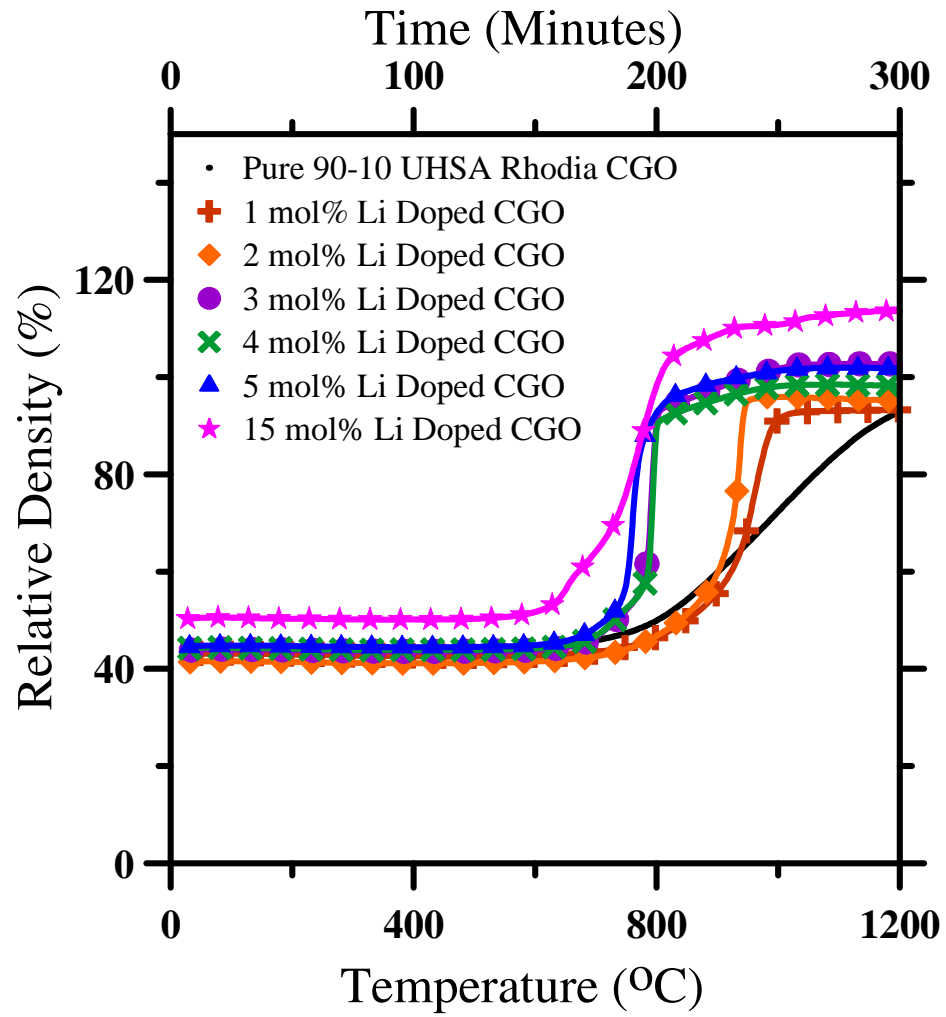
Figure 24- Dilatometry of CGO Doped with Lithium Salts at the 3mol% Level
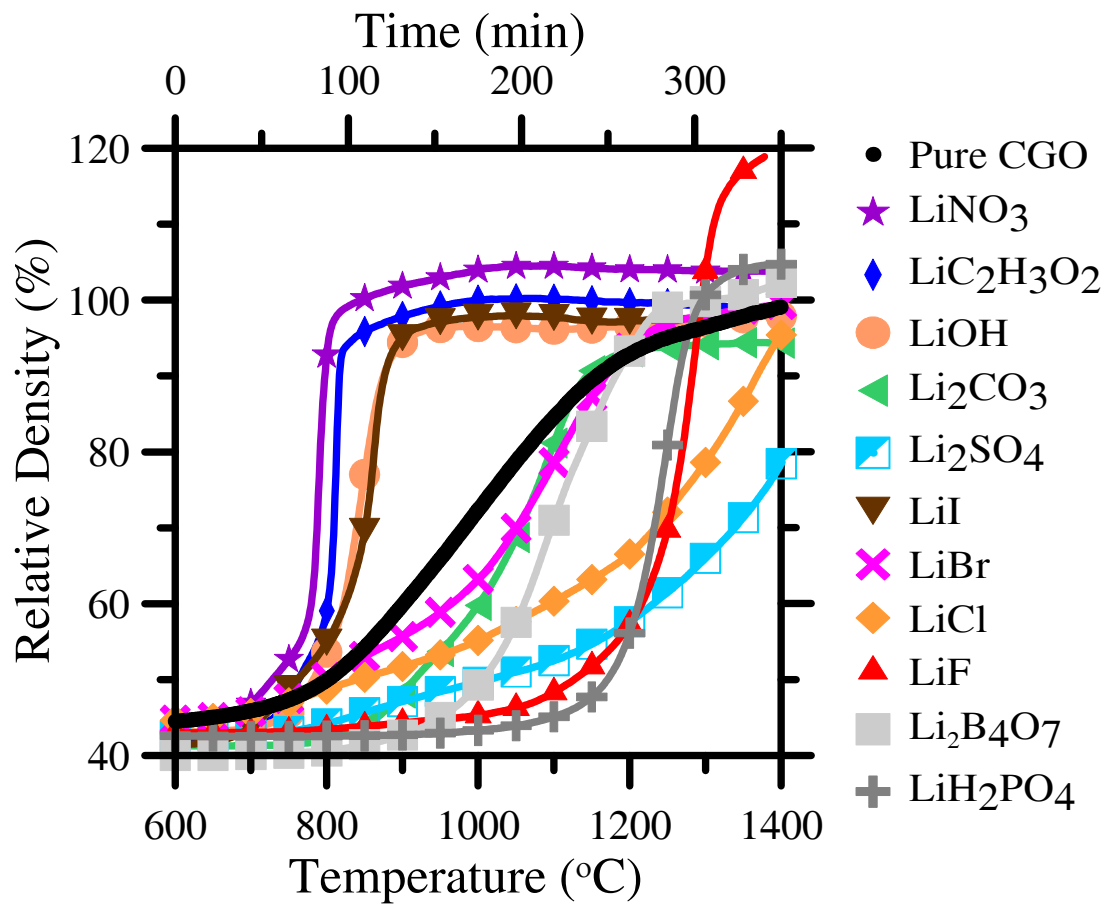
Figure 25- Total Conductivity of 3mol% Li-CGO fired to 800°C for 1 hr

Pure $Ce_{0.9}G_{0.1}O_{1.95}$ data from Kharton et al.[32], Huang et al.[59], Zhou et al. [60], and this study appear as straight lines. The initial 3mol% Li-CGO test is represented by triangles. The 3mol% Li-CGO retest taken the subsequent day after the sample's electrodes were removed by sanding and new electrodes were reapplied are represented by circles.
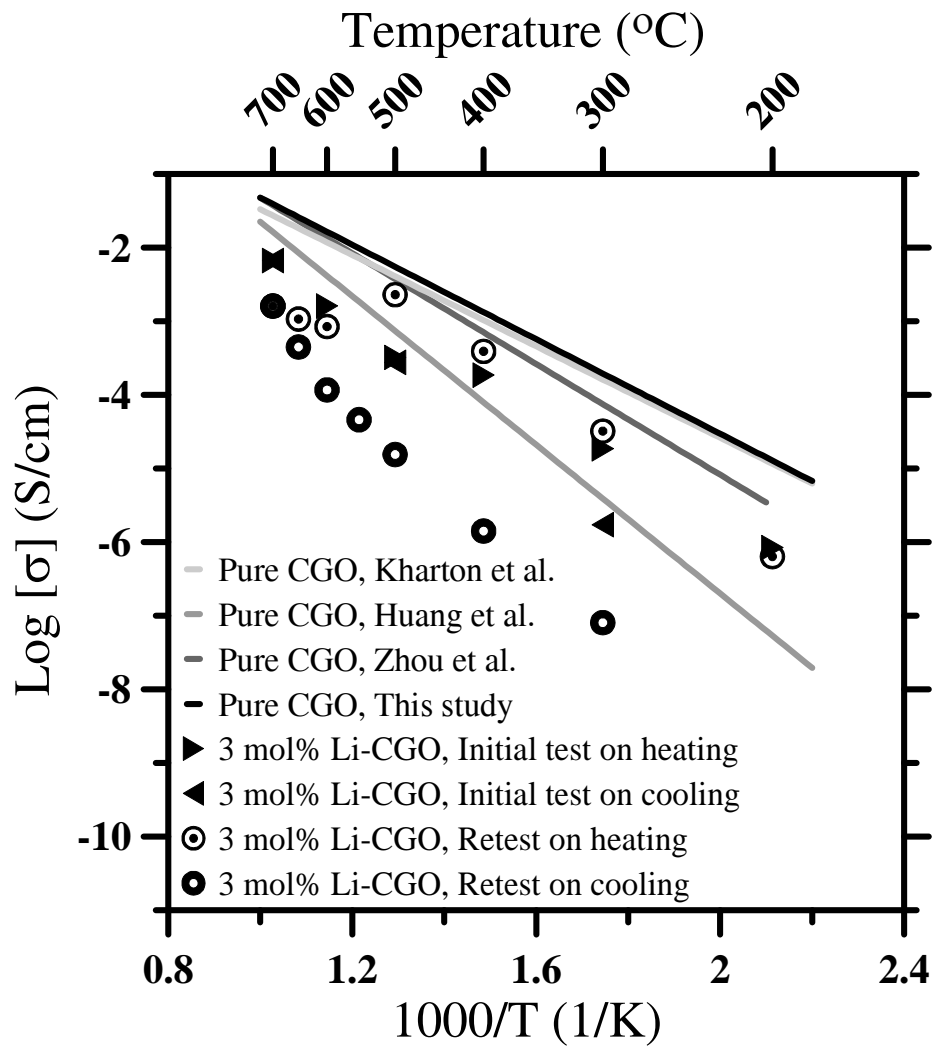
Figure 26- Microstructure of Pure CGO Fired at 1400°C

Sample was polished and thermally etched at 1300°C for 20 minutes.
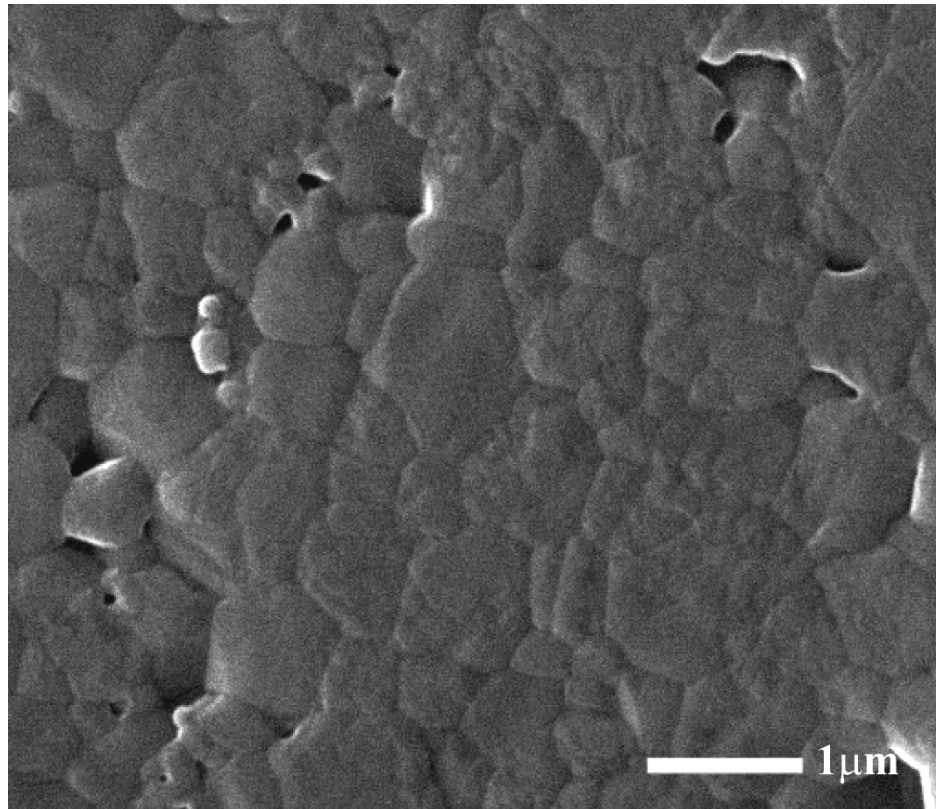
Figure 27- Microstructure of 3mol% LiNO₃ doped CGO Fired at 1400°C

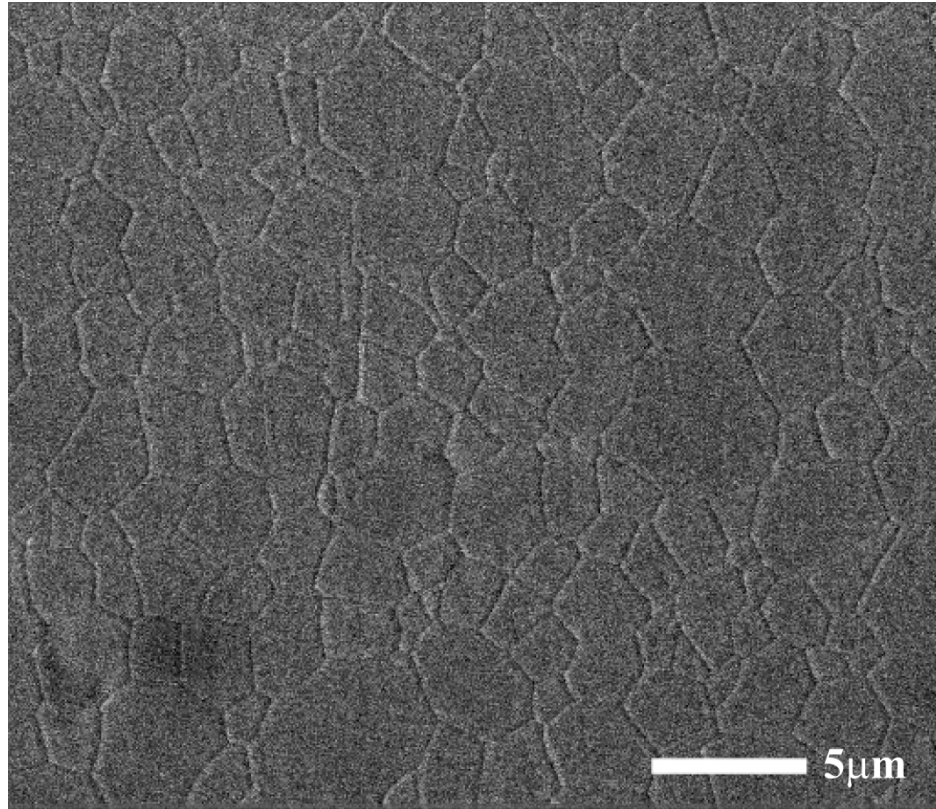Sample was polished and thermally etched at 1300°C for 20 minutes.

Figure 28- SEM Micrograph of 3mol% LiNO₃ doped CGO heated to 800°C

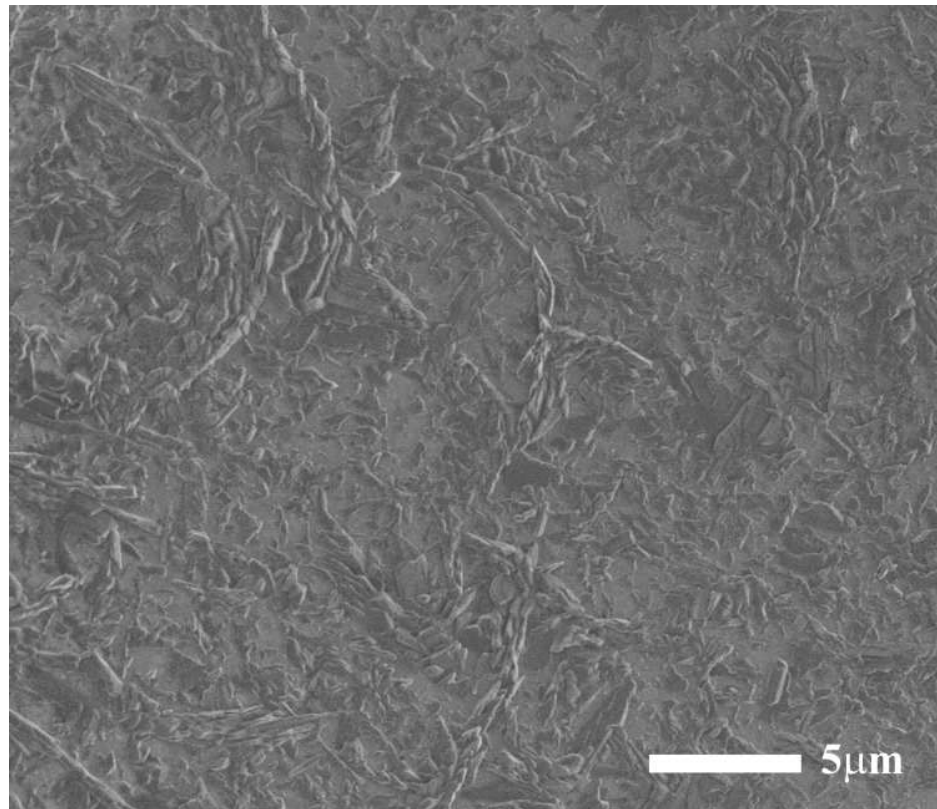Sample was polished and thermally etched at 750°C for 20 minutes.

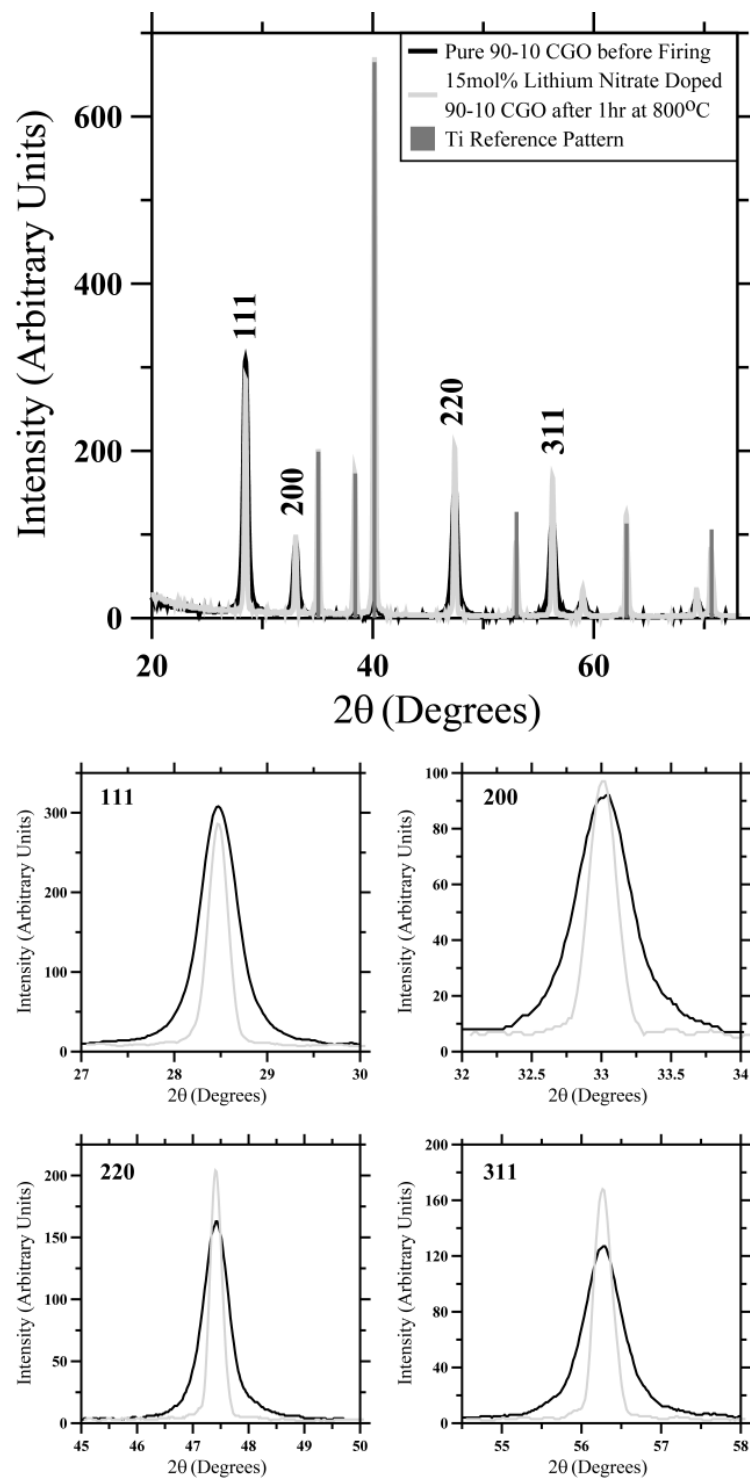**Figure 29- XRD Scan of Pure and 15mol% Li-CGO**

Figure 30- TEM of Pure CGO Fired for 1 hr at 800°C in a Li Saturated Atmosphere

Approximately 2/3 of the grain boundaries were clean, as seen in part a, and 1/3 of the grain boundaries had amorphous intergrannular films, as shown in parts b and c.
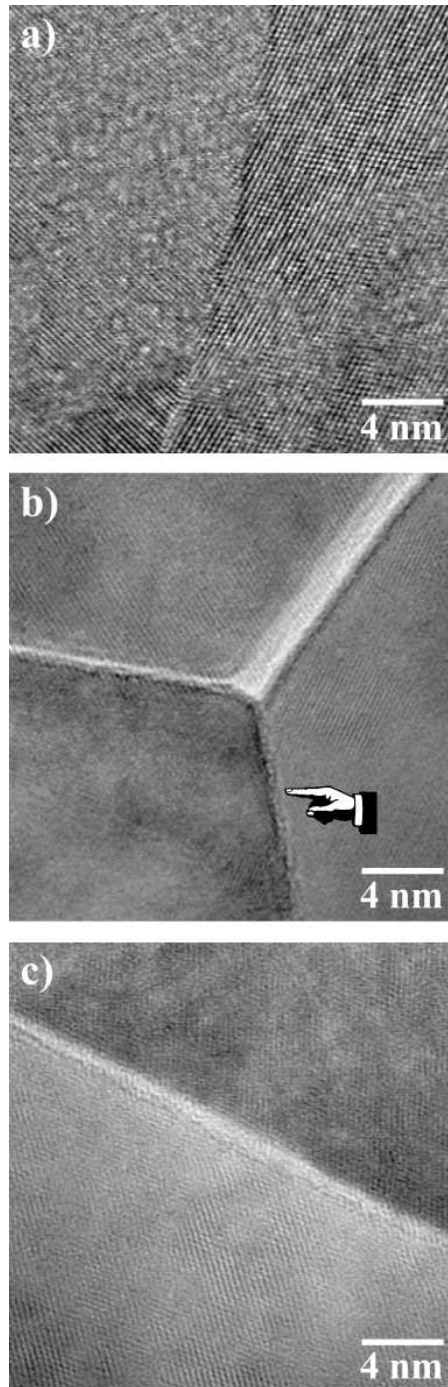
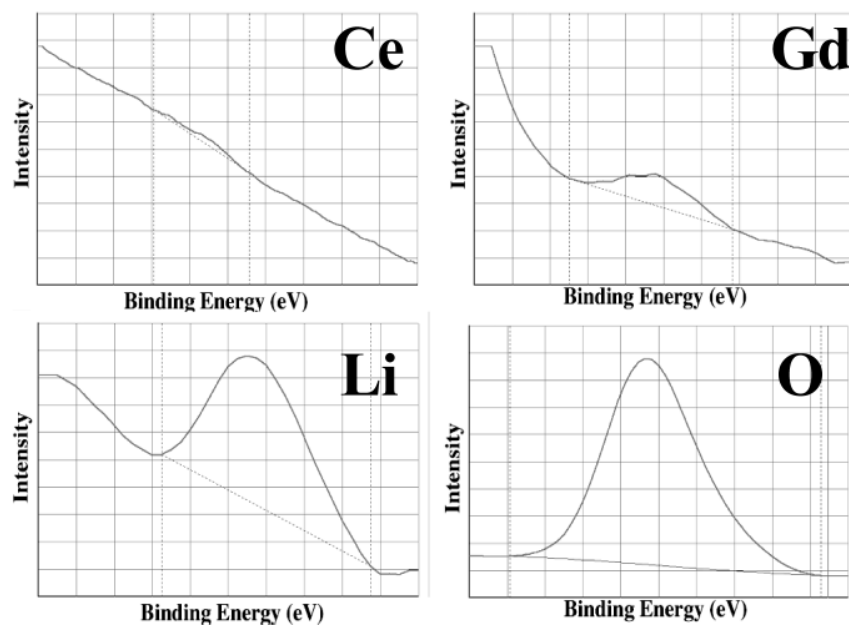**Figure 31- XPS of the Clear Phase atop 15mol% Li-CGO Fired to 800°C for 1 hr**

Figure 32- Cross Section of a Pure Constrained CGO Film Fired to 1400°C for 4 hrs.
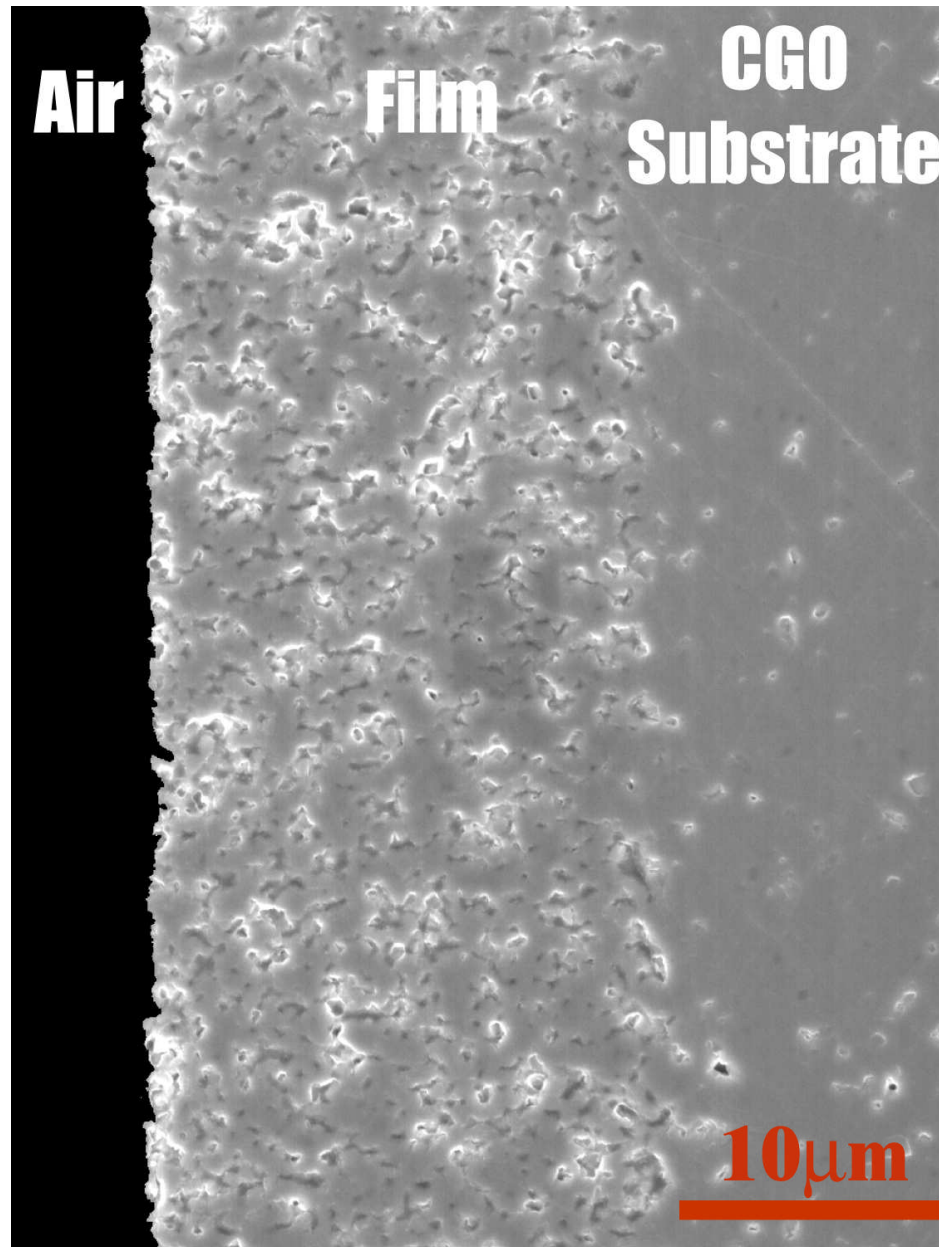
Figure 33- Temp.-Time Processing Map for Constrained 3mol% Li-CGO Films
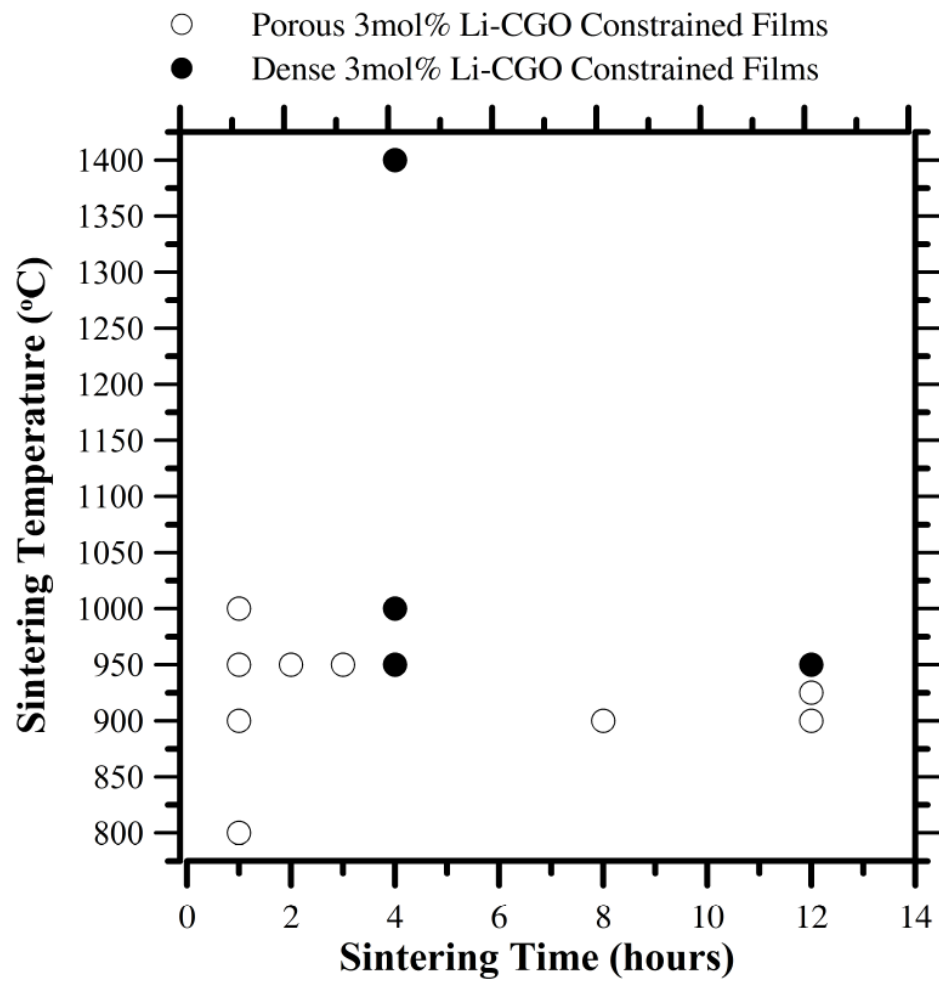
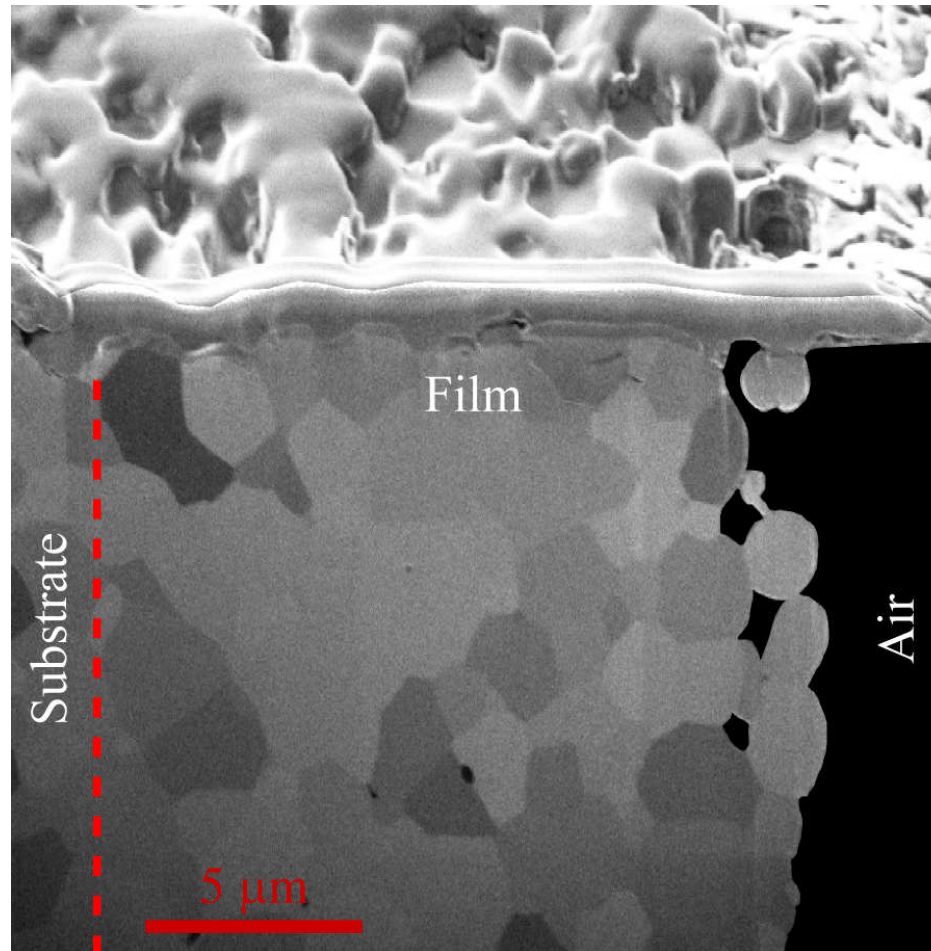**Figure 34- FIB Cross Section of 3mol% Li-CGO Fired at 950°C for 4 hrs.**

Figure 35- 3mol% Li-CGO Total Conductivity After Multiple Li Removal Attempts
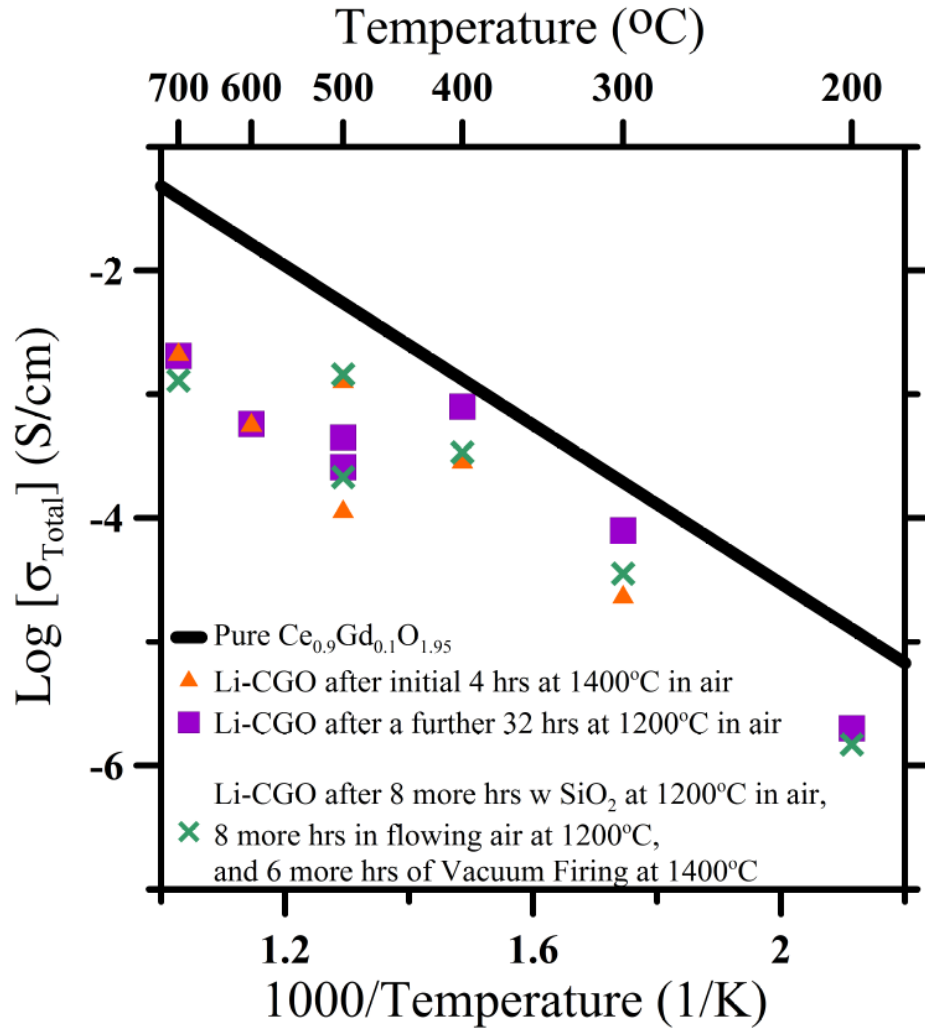
Figure 36- Conductivity of an Un-pressed, Constrained 3mol% Li-CGO Film

Fired in a Li Unsaturated Atmosphere at 1100°C for 4 hrs. Arrows indicate data collection path.
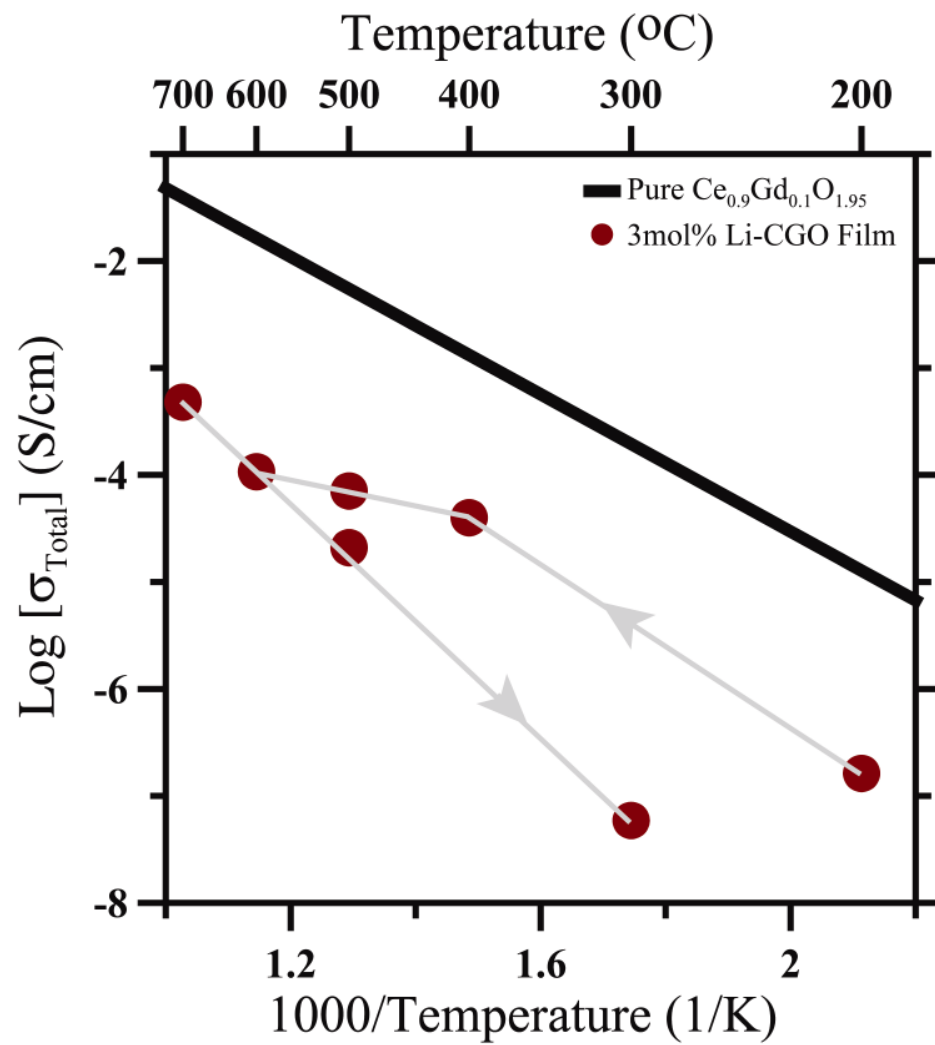
Figure 37- Dopant Decomposition Temp. vs. the Maximum Strain Rate Temp.

Maximum Strain Rate Temperature were determined from dilatometry data. Dopant Decomposition Temperatures were calculculated assuming the relevant partial pressures of to be pO2=0.2atm, pCO2=0.0033atm, and pBr2~pI2~pCl2~pF2~1x10-12 atm [61]. The thermodynamic data used for the calculations came from Refs.[54, 62] Note, that LiI and LiBr were omitted, even though they decompose at elevated temperature, because they are metastable in air for all temperatures used in this study. LiCl, LiF, $Li_2B_4O_7$ and LiH_2PO_4 were omitted because they are stable in air for all temperatures used in this study.
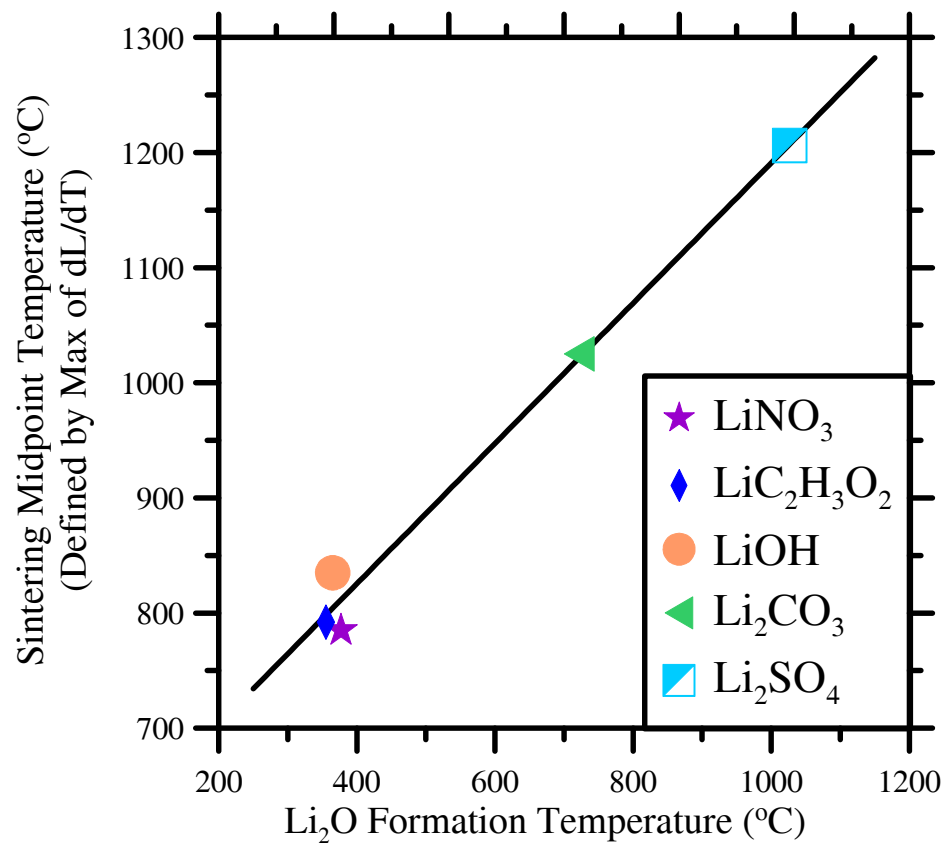
References

1. http://www.fossil.energy.gov/programs/powersystems/fuelcells/ fuelcells_solidoxide.html, Tubular Solid Oxide Fuel Cell Technology, U.S. Department of Energy (2006).

2. http://www.fe.doe.gov/programs/powersystems/gasification/index.html, Gasification Technology R&D, U.S. Department of Energy (2006).

3. B.C.H. Steele and A. Heinzel, *Nature* **414** (2001), p. 345.

4. C. Kleinlogel and L.J. Gauckler, *Advanced Materials* **13** (2001) (14), p. 1081.

5. N.P. Brandon, D. Corcoran, D. Cummins, A. Duckett, K. El-Khoury, D. Haigh, R. Leah, G. Lewis, N. Maynard, T. McColm, R. Trezona, A. Selcuk and M. Schmidt, *Journal of Materials Engineering and Performance* **13** (2004) (3), p. 253.

6. S.M. Haile, *Acta Materialia* **51** (2003), p. 5981.

7. N. Oishi, A. Atkinson, N.P. Brandon, J.A. Kilner and B.C.H. Steele, *Journal of the American Ceramic Society* **88** (2005) (6), p. 1394.

8. J.-S. Lee, K.-H. Choi, B.-K. Ryu, B.-C. Shin and I.-S. Kim, *Ceramics International* **20** (2004), p. 807.

9. V. Gil, J. Tartaj, C. Moure and P. Duran, *Journal of the European Ceramic Society* **27** (2007), p. 801.

10. E. Jud, Z. Zhang, W. Sigle and L.J. Gauckler, *Journal of Electroceramics* **16** (2006), p. 191.

11. D.P. Fagg, V.V. Kharton and J.R. Frade, *Journal of Electroceramics* **9** (2002), p. 199.

12. G.S. Lewis, A. Atkinson, B.C.H. Steele and J. Drennan, *Solid State Ionics* **152-153** (2002), p. 567.

13. M. Mori, E. Suda, B. Pacaud, K. Murai and T. Moriga, *Journal of Power Sources* **157** (2006), p. 688.

14. D. Perez-Coll, P. Nunez, J.C.C. Abrantes, D.P. Fagg, V.V. Kharton and J.R. Frade, *Solid State Ionics* **176** (2005), p. 2799.

15. T.S. Zhang, J. Ma, Y.J. Leng, S.H. Chan, P. Hing and J.A. Kilner, *Solid State Ionics* **168** (2004), p. 187.

16. T. Zhang, P. Hing, H. Huang and J. Kilner, *Materials Letters* **57** (2002), p. 507.

17. T.S. Zhang, J. Ma, S.H. Chan and J.A. Kilner, *Solid State Ionics* **176** (2005), p. 377.

18. T.S. Zhang, J. Ma, L.B. Kong, S.H. Chan, P. Hing and J.A. Kilner, *Solid State Ionics* **167** (2004), p. 203.

19. T.S. Zhang, J. Ma, L.B. Kong, P. Hing, Y.J. Leng, S.H. Chan and J.A. Kilner, *Journal of Power Sources* **124** (2003), p. 26.

20. T.S. Zhang, J. Ma, L.B. Kong, Z.Q. Zeng, P. Hing and J.A. Kilner, *Materials Science and Engineering B* **103** (2003), p. 177.

21. J.-S. Lee and K.-H. Choi, *Journal of Materials Science* **40** (2005), p. 1153.

22. C.Y. Kang, H. Kusaba, H. Yahiro, K. Sasaki and Y. Teraoka, *Solid State Ionics* **177** (2006), p. 1799.

23. E. Jud and L. Gauckler, *Journal of the American Ceramic Society* **89** (2006) (9), p. 2970.

24. C. Herring, *Journal of Applied Physics* **21** (1950), p. 301.

25. P.-L. Chen and I.-W. Chen, *Journal of the American Ceramic Society* **79** (1996) (7), p. 1793.

26. D.-J. Kim, *Journal of the American Ceramic Society* **72** (1989) (8), p. 1415.

27. S.J. Hong and A.V. Virkar, *Journal of the American Ceramic Society* **78** (1995) (2), p. 433.

28. J. Ranlov, F.W. Poulsen and M. Mogensen, *Solid State Ionics* **61** (1993), p. 277.

29. R. Gerhardt, A.S. Nowick, M.E. Mochel and I. Dumler, *Journal of the American Ceramic Society* **69** (1986) (9), p. 647.

30. W.D. Kingery, *Journal of Applied Physics* **30** (1959) (3), p. 301.

31. P.-L. Chen and I.-W. Chen, *Journal of the American Ceramic Society* **77** (1994) (9), p. 2289.

32. V.V. Kharton, F.M. Figueiredo, L. Navarro, E.N. Naumovich, A.V. Kovalevsky, A.A. Yaremchenko, A.P. Viskup, A. Carneiro, F.M.B. Marques and J.R. Frade, *Journal of Materials Science* **36** (2001), p. 1105.

33. C. Kleinlogel and L.J. Gauckler, Nano Sized Ceria Solid Solutions for Intermediate Temperature Solid Oxide Fuel Cells, In: S.C. Singhal and M. Dokiya, Editors, *SOFC VI*, Electrochemical Society, Honolulu, Hawaii, USA (1999), pp. 225-232.

34. P.J. Linstrom and W.G. Mallard, Editors, *NIST Chemistry WebBook, NIST Standard Reference Database Number 69*, National Institute of Standards and Technology, Gaithersburg, MD (2005).

35. K. Wieczorek-Ciurowa and A.J. Kozak, *Journal of Thermal Analysis and Calorimetry* **58** (1999), p. 647.

36. A.K.H. Nohman, H.M. Ismail and G.A.M. Hussein, *Journal of Analytical and Applied Pyroylsis* **34** (1995), p. 265.

37. H.J. Avila-Paredes and S. Kim, *Solid State Ionics* **177** (2006), p. 3075.

38. M.N. Rahaman and Y.C. Zhou, *Journal of the European Ceramic Society* **15** (1995), p. 939.

39. L.A. Chick, L.R. Pederson, G.D. Maupin, J.L. Bates, L.E. Thomas and G.J. Exarhos, *Materials Letters* **10** (1990), p. 6.

40. R.D. Shannon, *Acta Cryst.* **A32** (1976), p. 751.

41. E. Jud, C.B. Huwiler and L.J. Gauckler, *Journal of the American Ceramic Society* **88** (2005) (11), p. 3013.

42. J. Drenan, D.R. Clarke, R.H.J. Hannink and T.M. Shaw, *Journal of the American Ceramic Society* **77** (1994) (8), p. 2001.

43. G.W. Scherer and T. Garino, *Journal of the American Ceramic Society* **68** (1985) (4), p. 216.

44. H.B. Li, C.R. Xia, X.H. Fang, X. He, X.L. Wei and G.Y. Meng, *Key Engineering Materials* **280-283** (2005), p. 779.

45. G. Schiller, R. Henne, M. Lang and M. Muller, *Materials Science Forum* **426** (2003) (4), p. 2539.

46. B.C.H. Steele, G. Lewis, N. Oishi and A. Selcuk, Densification of Ceria Based Electrolytes-Patent Number WO 2004/089848 A1, *World Intellectual Property Organization*, B.C.H. Steele, United Kingdom (2004).

47. T. Zhang, P. Hing and H. Huang, *Journal of Materials Science* **37** (2002), p. 997.

48.   P.E. Hart, R.A. Atkin and J.A. Pask, *Journal of the American Ceramic Society* **52** (1970) (2), p. 83.

49.   D.R. Linde, Editor, *CRC Handbook of Chemistry and Physics*, CRC Press, Boca Raton, FL (2000).

50.   M. Marrero-Cruz, E.P. Hong, C.P. Jacobson, S.J. Visco and L.C. DeJonghe, Processing and Properties of Thin-Film Ceria Based SOFC, In: S.C. Singhal and M. Dokiya, Editors, *SOFC VIII*, Electrochemical Society, Pennington NJ USA, Paris, France (2003), pp. 253-260.

51.   S. DeSouza, S.J. Visco and L.C. DeJonghe, *Solid State Ionics* **98** (1997), p. 57.

52.   R.H. Lamoreaux, D.L. Hildenbrand and L. Brewer, *Journal of Chemical Reference Data* **16** (1987) (3), p. 419.

53.   R.H. Lamoreaux and D.L. Hildenbrand, *Journal of Chemical Reference Data* **13** (1984) (1), p. 151.

54.   M.W. Chase, *Journal of Physical Chemical Reference Data, Monograph 9* (1998), p. 1.

55.   R.T. Grimley, R.P. Burns and M.G. Inghram, *Journal of Chemical Physics* **45** (1966) (11), p. 4158.

56.   R.T. Grimley, R.P. Burns and M.G. Inghram, *Journal of Chemical Physics* **35** (1961) (2), p. 551.

57.   W.D. Halstead, *Corrosion Science* **15** (1975), p. 603.

58.   L. Brewer and D.F. Mastick, *Journal of Chemical Physics* **19** (1951) (7), p. 834.

59.   K. Huang, M. Feng and J.B. Goodenough, *Journal of the American Ceramic Society* **81** (1998) (2), p. 357.

60. X.-D. Zhou, W. Huebner, I. Kosacki and H.U. Anderson, *Journal of the American Ceramic Society* **85** (2002) (7), p. 1757.

61. B.D. Finley and E.S. Saltzman, Observations of Cl2, Br2, and I2 in Coastal Urban Air, *American Geophysical Union Fall Meeting*, San Francisco, CA (2006).

62. I. Barin, *Thermochemical Data of Pure Substances*, VCH, New York (1995).